Journal of Rock Mechanics and Geotechnical Engineering 17 (2025) 71–93

Contents lists available at ScienceDirect

Journal of Rock Mechanics and Geotechnical Engineering

journal homepage: www.jrmge.cn

Full Length Article

Large-scale laboratory investigation of pillar-support interaction

Akash Chaurasia [a, *], Gabriel Walton [a], Sankhaneel Sinha [a, b], Timothy J. Batchler [c], Kieran Moore [d], Nicholas Vlachopoulos [d], Bradley Forbes [e]

[a] Colorado School of Mines, Golden, CO, USA
[b] Equilibrium Mining, Kolkata, West Bengal, India
[c] National Institute of Occupational and Safety Hazard (NIOSH), Pittsburgh, PA, USA
[d] Royal Military College of Canada (RMC), Kingston, Ontario, Canada
[e] BGC Engineering Inc., Kingston, Ontario, Canada

ARTICLE INFO

Article history:
Received 18 October 2023
Received in revised form
1 March 2024
Accepted 14 April 2024
Available online 8 June 2024

Keywords:
Grouted rockbolt
Welded wire mesh
Porous limestone
Digital image correlation
Distributed fiber optic sensing
Large-scale laboratory tests

ABSTRACT

Underground mine pillars provide natural stability to the mine area, allowing safe operations for workers and machinery. Extensive prior research has been conducted to understand pillar failure mechanics and design safe pillar layouts. However, limited studies (mostly based on empirical field observation and small-scale laboratory tests) have considered pillar-support interactions under monotonic loading conditions for the design of pillar-support systems. This study used a series of large-scale laboratory compression tests on porous limestone blocks to analyze rock and support behavior at a sufficiently large scale (specimens with edge length of 0.5 m) for incorporation of actual support elements, with consideration of different *w/h* ratios. Both unsupported and supported (grouted rebar rockbolt and wire mesh) tests were conducted, and the surface deformations of the specimens were monitored using three-dimensional (3D) digital image correlation (DIC). Rockbolts instrumented with distributed fiber optic strain sensors were used to study rockbolt strain distribution, load mobilization, and localized deformation at different *w/h* ratios. Both axial and bending strains were observed in the rockbolts, which became more prominent in the post-peak region of the stress-strain curve.

1. Introduction

Pillar mechanics and design have been extensively studied in the field of mining engineering. Empirical studies, laboratory testing, and numerical modeling have been used to design pillars and investigate deformation behavior under various loading conditions. However, these methods have unique strengths and weaknesses in their ability to provide broadly applicable insights. For instance, common empirical pillar design methods only consider the pillar load and peak strength, and neglect the effects of post-peak behavior, and rock-support interaction (Obert et al., 1946; Bieniawski, 1968; Lunder and Pakalnis, 1997; Martin and Maybee, 2000). Laboratory tests can provide information regarding pillar failure mechanics under various controlled conditions, but they are generally conducted on small-scale specimens and the upscaling of the results to the field scale is not straightforward (Das, 1986; Medhurst and Brown, 1998; Li et al., 2011; Zhou et al., 2018). Both continuum and discontinuum numerical modeling methods are used to study the strength and deformation behavior of pillars at small and large scales, but there remain uncertainties regarding the calibration and validation of such models (Hajiabdolmajid et al., 2003; Jaiswal and Shrivastva, 2009; Ghazvinian et al., 2014; Bahaaddini and Rahimi, 2018; Walton and Sinha, 2022).

Even if pillar geometries are effectively designed to limit the potential for global instability (i.e. complete pillar failure), local instability issues such as progressive spalling and rock slabbing from pillar walls can occur, posing risks of worker injuries and machinery damage. Support systems, such as rockbolts, wire mesh, face plates, and shotcrete are frequently employed to enhance pillar integrity by reinforcing unstable blocks or by containing the loosened rocks around the periphery. However, pillar-support system design often relies largely on field experience, which is applicable

* Corresponding author.
E-mail address: achaurasia@mines.edu (A. Chaurasia).
Peer review under responsibility of Institute of Rock and Soil Mechanics, Chinese Academy of Sciences.

https://doi.org/10.1016/j.jrmge.2024.04.008

to specific geological conditions but lacks consideration of the micro-mechanical interaction between rock and support (e.g. Colwell and Mark, 2005; Colwell, 2006; Mohamed et al., 2016). This may lead to a limited understanding of the true stability of a pillar and its potential responses during pre- and post-peak loading stages. Consequently, it contributes to a conservative pillar-support design, thereby increasing the overall project cost.

In the context of rock-support interaction specifically, analytical models have been developed to understand the mechanical response of independent support components (e.g. Hyett et al., 1996; Li and Stillborg, 1999; Ma et al., 2013) but may be inadequate for evaluation of combinations of different supports (combined wire mesh, face plate, and rockbolt). Laboratory tests, whether on large-scale specimens or in situ conditions, have aimed to understand the micro-mechanical response of the support system (e.g. Serbousek and Signer, 1987; Grasselli, 2005; Vlachopoulos et al., 2018). However, these studies focus primarily on pull or shear tests, neglecting the complex loading mechanisms experienced during stress-induced in situ fracturing. Alejano et al. (2017) conducted uniaxial compressive tests on small-scale limestone and granite specimens to examine the effects of cable strapping on a 54 mm diameter core. While their study provides insight into rock-support interaction, it was limited to consideration of cable straps and slender specimens ($w/h = 0.5$). Moreover, the upscaling of these behaviors to the field is not well-understood. Numerical tools are often used to understand the pillar-support interaction and to recommend the support design guidelines, but these models are often calibrated with a limited data set, either under ideal loading conditions or using an empirical database, leading to uncertainty regarding the validation and predictive capabilities of the model (Lorig and Varona, 2013; Gao et al., 2015; Bahrani and Hadjigeorgiou, 2017; Bai and Tu, 2020).

In this study, we apply an alternative approach for the study of pillar mechanics and rock-support interaction. Specifically, large-scale laboratory tests were employed to enable the use of controlled conditions while allowing for incorporation of full-scale support elements (rockbolts, wire mesh, and face plate), such that the results can be more easily extrapolated to the field scale or in-situ pillars without significant concerns regarding scale effects. With that in mind, different support element configurations were tested to evaluate their effects on overall pillar stress-strain behavior for multiple pillar geometries, as well as to study support loading mechanisms in these various scenarios. Regarding the latter, rockbolts were instrumented with a high spatial resolution distributed fiber optic sensing (DOS) technique to measure element load mobilization and reinforcement mechanisms within the rock samples.

2. Background

2.1. Pillar damage mechanisms

Small-scale laboratory tests under compressive load (Martin and Chandler, 1994; Cai et al., 2004) and field studies (Martin, 1997; Diederichs, 2007; Andersson et al., 2009) have been conducted to study the progressive failure of brittle rock and have been linked to understanding pillar failure mechanisms. Through laboratory tests, the failure process of an intact rock can be characterized into five different stages: crack closure, crack initiation (CI), crack damage (CD), peak, and residual. Crack closure is associated with the deformation of pre-existing microcracks. Under further loading, tensile cracks start to form parallel to the uniaxial stress direction, at the CI threshold. These tensile cracks coalesce with each other to form shear fractures following the CD threshold. Ultimately, a macroscopic failure plane is generated, and the rock achieves its peak strength. After attaining the peak strength, the rock continues to deform more under loads below the peak strength. Eventually, a constant residual stress state corresponding to the residual strength is reached.

At the field scale, extensile cracks form at the pillar periphery due to the high tangential and low confining stresses (Diederichs and Kaiser, 1999). As such, macroscopic spalling is observed at the boundary, and this generally occurs at the CI threshold. As one moves toward the center of the pillar, the confining stress increases, and the prevalence of extensile cracks decreases; therefore, a larger stress (greater than the CD threshold also known as short-term strength) is required for cracks to propagate, and failure occurs through shear damage. The shear damage mechanism is typically observed in pillars with higher w/h ratios, where a relatively higher confining stress is generated in the pillar core (Kaiser et al., 2011).

2.2. Rock support mechanisms

Rock support plays a vital role in providing stability to underground/surface excavations and creating safe conditions for workers. Rockbolts, cable bolts, and wire meshes are common wall and roof support types in underground excavations. Kaiser et al. (1996) presented three primary functions of rock support: (a) reinforcement: strengthening the rockmass so that it can support itself, generally achieved using rockbolts; (b) retaining: keeping together the broken rock to prevent progressive failure, typically using concrete liner or wire mesh; and (c) holding: anchoring the retaining support elements to the stable ground.

Fully grouted rockbolts are commonly used to provide stability to the rockmass in both underground and surface excavation contexts. This type of rockbolt is also referred to as a continuous mechanically coupled (CMC) rockbolt, where the element is generally inserted into a predrilled borehole, encapsulated with cement or resin grout along the entire length, and pretensioned using external fixtures such as a face plate and nut (Windsor, 1997). Under load/deformation, the bond at the rockbolt-grout interface is created through the mechanical interlock between the rebar ribs and grout and the weak adhesion between them, whereas the bond at the grout-rock interface is due to the roughness (i.e. frictional mobilization) of the borehole surface. Failure of the fully grouted rockbolt generally occurs through a combination of failure of the rockbolt-grout interface, failure of the grout-rock interface, or bolt yield. The rockbolt itself yields and undergoes plastic deformation when the axial stress exceeds the yield strength of the rockbolt and generally fails through necking when the tensile strain reaches the rupture strain limit. The rockbolt-grout or grout-rock interface fails when the shear stress generated at the interface due to the axial stress in the rockbolt exceeds the bond strength (either for rockbolt-grout or grout-rock interface) (Hyett et al., 1996).

During pillar loading, axial loads are induced on the rockbolt due to lateral spalling/dilation of rocks. Additionally, localized bending can occur along the rockbolt due to differential unbalanced lateral loading induced by the shear movement of the fractures. Fig. 1 shows the different components of the forces generated on a rockbolt section AB due to lateral and shear fractures in an axially loaded pillar. Shear stress is generated at the rockbolt-grout interface to counter the axial stress in the rockbolt. Details regarding the evaluation of interface shear stress are provided by Li and Stillborg (1999). This paper primarily focuses on the deformation behavior (axial and bending) of rockbolts installed in specimens with different w/h ratios. Other factors, such as rockbolt geometry, rib spacings, grout material, and grout annulus, also influence bolt performance, but their effects have not been considered in this paper. Readers can refer to Vlachopoulos et al. (2018) and Moore and Vlachopoulos (2023) for additional details on these effects.

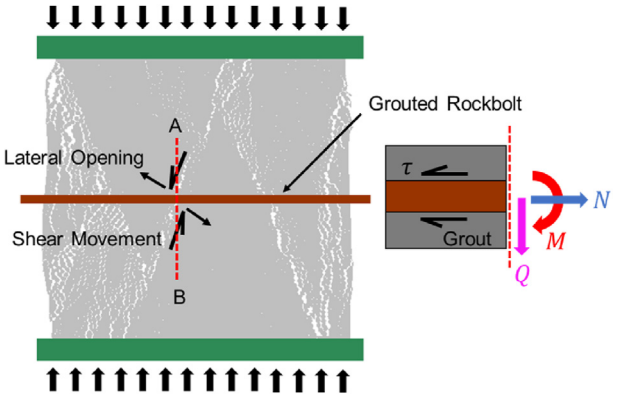

Fig. 1. A schematic of fully encapsulated grouted rockbolt illustrating the various loads generated on section AB due to the lateral and shear movement of the fractures in the pillar under compressive load (N is the axial load, M is the bending moment, Q is the lateral load, and τ is the shear stress on the bolt-grout interface).

Rockbolts generally constrain the deformation of the rock mass along their length within a specific zone of influence. Therefore, surface support such as wire mesh is used in conjunction with rockbolts to contain the spalled material from the excavation surface and provide additional confinement to the rock mass. The connection between the rockbolt and wire mesh is established through a face plate attached at the end of the bolt thread with a nut. This paper will also discuss the effects of face plates and wire mesh on rock deformation.

2.3. Working principle of three-dimensional digital image correlation

DIC is an optical method used to calculate two-dimensional (2D) and three-dimensional (3D) full-field displacement and strain by analyzing images taken at specific intervals of the specimen under testing. The coordinates of displaced specimens are computed by correlating the pixel subset of the images before and after deformation. The undeformed stage of the rock specimen serves as the reference image. The reference image is divided into a small group of pixels called a subset using a facet size, and the distance between the subsets is defined by the point distance. Random speckle patterns are created on the specimen surface, typically through paint spraying. A group of speckles (typically 4–5) is combined to form a subset. The DIC method tracks these subsets in the deformed stages to compute the new coordinates of the initial subsets. The displacement is calculated based on the camera distances from the specimen and the subset's new coordinates (Sutton et al., 2009). Strain is computed from the displacement field using Lagrangian continuum mechanics. The 2D-DIC method uses a single camera to calculate the in-plane deformation of a planar object surface (Pan et al., 2009), whereas 3D-DIC uses a stereo camera to compute the in-plane and out-of-plane deformation of a 3D object.

2.4. Working principle of fiber optic sensing

A fiber optic sensor uses optical fiber to measure strain, vibration, temperature, pressure, velocity, and torque, depending on the interrogation technique and sensor arrangement. Optical fiber is composed of a glass or plastic core surrounded by a cladding material with a lower refractive index (Fig. 2). Buffer and jacket layers add strength to the cable and prevent damage due to high stress. Light traveling through the fiber reflects from the core-cladding boundary due to total internal reflection. This phenomenon results in the transmission of all rays that enter the fiber. However, a physical change to the optical fiber (e.g. due to the temperature and strain changes) alters the propagating signals and shifts the amplitude, frequency, intensity, and input signal phase. Various interrogation techniques exist to capture these changes and determine a relationship between them and the physical changes.

This research employs a DOS technique to measure strain. DOS relies on measuring changes in Rayleigh, Brillouin, and Raman scattering in the optical fiber to determine strain and temperature changes along the fiber length. Any alterations in strain and temperature will modify the scattered signal (frequency, amplitude). Optical time domain reflectometry (OTDR) and optical frequency domain reflectometry (OFDR) techniques are generally used to estimate the location and intensity of strain and temperature changes along the fiber.

Fiber optic sensors have a broad range of applications. This approach has been used in various industries to monitor strain and temperature over a range of sensing lengths. They are employed for monitoring electric power lines, bridges, pipelines, dams, landslides, tunnels, underground mines, and support systems (e.g. Hoepffner, 2008; Fidanboylu and Efendioglu, 2009). In the context of rock and support deformation, the selection of suitable fiber optic sensors for strain measurements depends on various parameters, such as operational features of the sensors, sensor cost, application, required accuracy, and sensor availability (Forbes et al., 2018).

Rayleigh optical frequency domain reflectometry (ROFDR) based sensors were chosen to capture the localized deformation behavior of the rock and rockbolt due to their high spatial resolution (0.65 mm). Forbes et al. (2017) have successfully implemented the ROFDR sensor in the support elements to study their axial and shear load behavior. They concluded that ROFDR is better suited

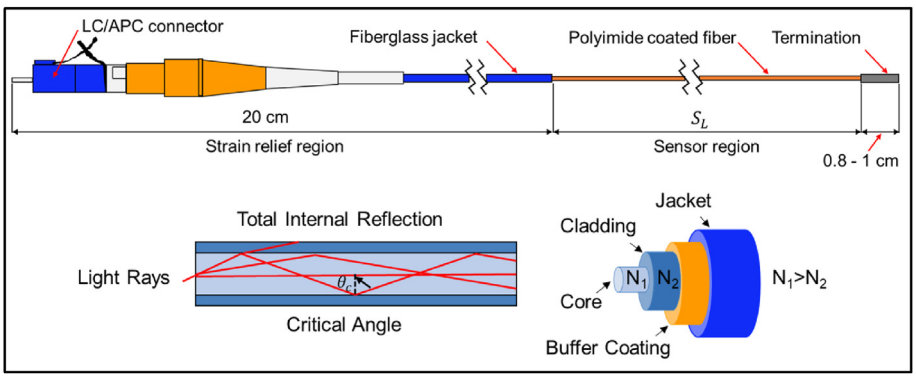

Fig. 2. A schematic view of fiber sensor with the description of different components and explanation of working mechanisms (after Luna Inc., 2023).

Table 1
Mechanical properties of Texas Cream Limestone obtained through standard Uniaxial Compressive Strength (UCS) and Brazilian Tensile Strength (BTS) tests (Sinha et al., 2022).

Item	UCS (MPa)	BTS (MPa)	Young's Modulus (GPa)	Poisson Ratio	Porosity
Value	13.9 ± 1.1	1.7 ± 0.2	10.9 ± 1.8	0.15 ± 0.03	26%

than discrete strain gauges and Fiber Bragg Grating (FBG) sensors in terms of spatial resolution and the associated low cost per meter of fiber length.

3. Experimental setup

3.1. Specimen description

Texas Cream Limestone is a lower Cretaceous (100.5–145 Ma) fossilized, light beige-cream white colored carbonate rock. It is classified as a grainstone based on Dunham's classification system (Dunham 1962) and is also known as Texas Beige Limestone or Tejas Cream Limestone. It is commonly used in interior wall and floor applications, fountains, countertops, and stairs. The specimens used in this study were purchased from New Mexico Travertine, a quarry company in New Mexico. The rock has a bulk density of approximately 2003 kg/m^3, suggesting a porosity of around 26%, assuming the specimen is composed of 100% calcite (with a grain density of 2708 kg/m^3). The basic mechanical properties obtained from a series of standard compression tests are summarized in Table 1 (Sinha et al., 2022).

Previously, compression tests were conducted on Texas Cream Limestone using cubic blocks ranging in size from 0.1 m to 0.9 m to evaluate the size effect on peak strength (Sinha et al., 2022). Additionally, uniaxial compression tests were conducted on square prismatic specimens with four different width-to-height (w/h) ratios, corresponding to small-scale pillar analogs. The cross-section of the specimens was kept constant at 15 cm × 15 cm, while the height was varied from 5 cm to 30 cm to achieve w/h ratios of 3, 2, 1, and 0.5 (Chaurasia and Walton, 2023). These studies did not consider the support elements during the tests.

This research considers further tests on square prismatic specimens with a constant cross-sectional area of 0.25 m^2 at three distinct w/h ratios (0.5, 1, and 2), as depicted in Fig. 3. In addition to the unsupported compressive tests, various support systems such as rockbolts and wire mesh were investigated at varying w/h ratios to gain insights into their impact on rock behavior. The full testing program for this study is summarized in Table 2.

3.2. Testing apparatus

Uniaxial compression tests were conducted using the Mine Roof Simulator (MRS) load frame located at the NIOSH, Pittsburgh facility. The MRS has a load capacity of 13.345 MN, allowing for a maximum stress of 53.4 MPa to be generated for the cross-section (0.25 m^2). Since no size effect on strength was observed for Texas Cream limestone (Sinha et al., 2022), and considering a potential doubling of strength between $w/h = 0.5$ and 2 (per Krauland and Soder, 1987), the Texas Cream limestone (UCS: 14 MPa) specimens could be successfully loaded up to and beyond peak strength using the MRS.

The upper and lower platens of the MRS measure 6.1 m × 6.1 m, and the vertical opening between them is 4.9 m. A load cell was used on the lower platen to raise the specimen, and the compressive load was applied via displacement control of the lower platen. Fig. 4 illustrates the MRS testing setup along with the 3D-DIC system. The lowest possible displacement rate (0.04 mm/s) was utilized to raise the lower plate of the MRS to allow for evaluation of the post-peak behavior. Further information about the MRS can be found in Barczak (2005).

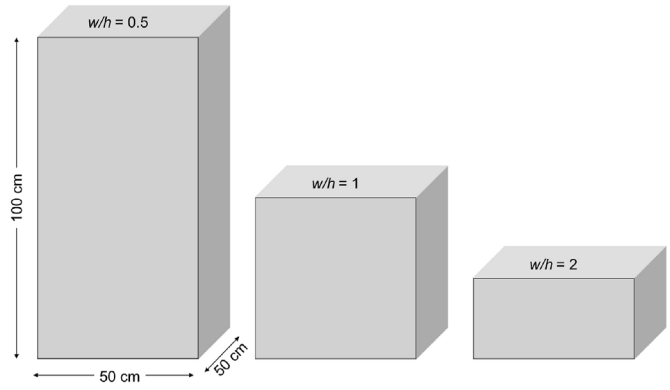

Fig. 3. Geometric shapes of Texas Cream Limestone at three different w/h ratios (0.5, 1, and 2) for large-scale compression tests.

3.3. Instrumentation arrangements

Apart from measuring vertical displacement with the built-in MRS linear variable differential transformer (LVDT), the surficial deformation of the specimens was monitored using the 3D-DIC system purchased from Trillion Quality Systems. The 3D-DIC system used for this testing program includes two 12 MP cameras (4096 × 3000 pixels) with a 35 mm focal length. The cameras were placed on an adjustable steel bar and mounted on a tripod. The height, distance, and angle between the cameras were adjusted to ensure that the center surface of the specimen was within the field of view. Polarizer lights were used to reduce glare and reflection during image acquisition. Images were captured at a rate of one frame per second with an aperture of $f/8$ using Trillion Snap software. To create the speckle pattern, the block surface was first painted white and then spray-painted with black color using low nozzle pressure. This allowed relatively large speckles to be obtained so that there were at least 5 pixels across every speckle as recommended by Trillion Quality System (2020). Before acquiring the images, camera calibration was performed by taking 13 images of the coded calibration panel at different distances and orientations. This was necessary to evaluate the camera angle, measuring volume, and height variance, and to reduce scale and calibration deviation. Once the 3D-DIC system was calibrated, images were acquired during the laboratory tests at 1-s intervals. Fig. 5 depicts the different components of the 3D-DIC system.

The DOS technique was used to monitor the local deformation of the unsupported specimens as well as the deformation of the rockbolts for the supported specimens. The ODiSI-B interrogation unit from Luna Innovations Inc. was used to obtain the strain data from the sensors at a spatial resolution of 0.65 mm. For the unsupported specimens, a fiber optic sensor was installed in the center of the specimen within a predrilled borehole. The fiber sensor was attached to the surface of a Poly Vinyl Chloride (PVC) pipe with a diameter of 6.3 mm using Loctite 401 adhesive (Fig. 6a). This adhesive is known for creating a high-strength bond with a fast cure time, making it suitable for metals, rubbers, and plastics

Table 2
Testing outline for Texas Cream limestone describing the testing type related to each *w*/*h* ratio.

Specimen ID	Testing type	Width (m)	Length (m)	Height (m)	*w*/*h* ratio	#Tests
U_0.5_i	Unsupported	0.5	0.5	1	0.5	2
UF_0.5_i	Unsupported with fiber sensors	0.5	0.5	1	0.5	2
WR_0.5_i	Single instrumented rockbolt with wire mesh	0.5	0.5	1	0.5	3
DR_0.5_i	Double instrumented rockbolt without face plate	0.5	0.5	1	0.5	3
U_1_i	Unsupported	0.5	0.5	0.5	1	1
UF_1_i	Unsupported with fiber sensors	0.5	0.5	0.5	1	2
R_1_i	Single instrumented rockbolt without face plate	0.5	0.5	0.5	1	2
WR_1_i	Single instrumented rockbolt with wire mesh	0.5	0.5	0.5	1	2
U_2_i	Unsupported	0.5	0.5	0.25	2	1
UF_2_i	Unsupported with fiber sensors	0.5	0.5	0.25	2	2
R_2_i	Single instrumented rockbolt without face plate	0.5	0.5	0.25	2	2

Note: For the Specimen ID, U is unsupported specimen; UF is unsupported with fiber sensors; WR is wire mesh with rockbolt and faceplates; DR is double rockbolt; R is rockbolt and the first subscript represents the *w*/*h* ratio and second subscript represent the test (where multiple tests were conducted for some samples).

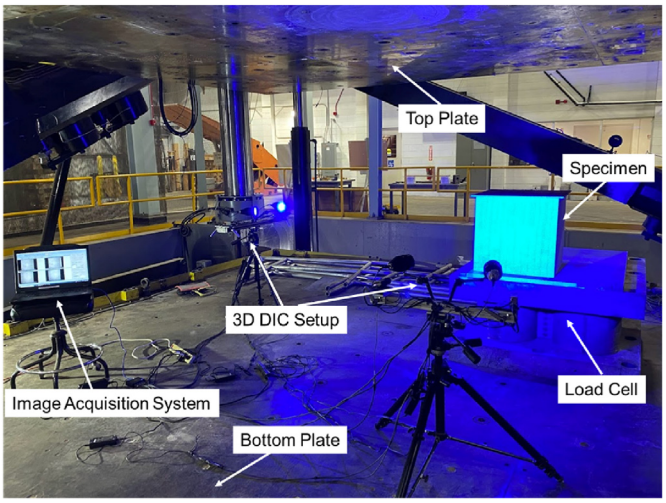

Fig. 4. MRS load frame setup for uniaxial compression tests, where the lateral surface was monitored by 3D-DIC.

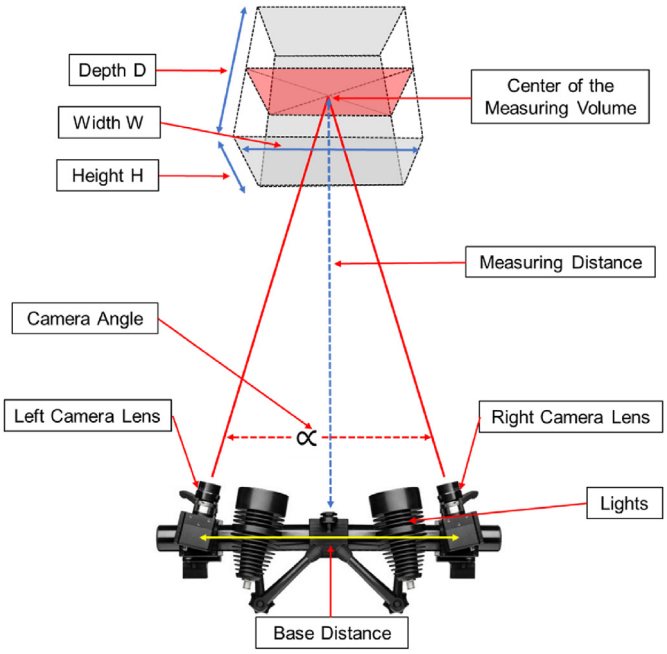

Fig. 5. An overview of the 3D-DIC system setup and detailed descriptions of its various components.

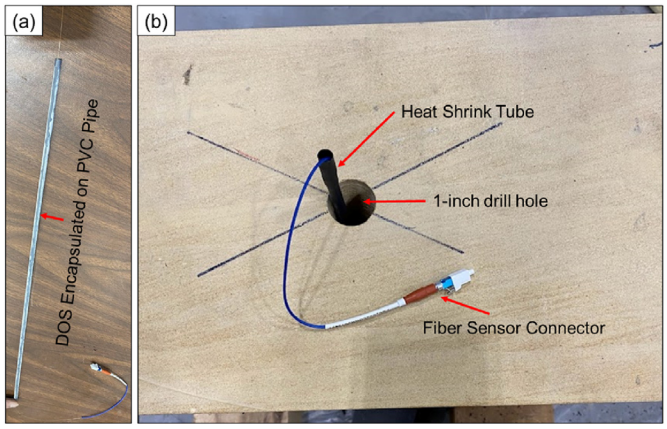

Fig. 6. (a) Attachment of the fiber sensor on a PVC pipe surface before grouting, and (b) 25.4 mm drill hole to grout the fiber sensor.

(Henkel Adhesive Technologies, 2012). The sensing length of the fiber sensor was 1 m; therefore, some portion of the sensing length remained outside the specimen. To ensure the protection of the connector and termination end of the sensor before grouting, heat-shrink tubes were applied using a heat gun. The specifications of the fiber optic sensor used for the unsupported specimens can be found in Luna Inc. (2023).

To install the unsupported specimen fiber sensors a pneumatic drill machine was used to create a 25.4 mm hole at the center of the specimens, allowing for at least a 9.5 mm grout annulus to encapsulate the sensor (Fig. 6b). Non-shrink precision grout from Quikrete was used to grout the sensors. The grout was mixed with water (mass ratio = 1:3) to achieve a fluid consistency, enabling direct pouring into the hole with the assistance of gravity. The compressive strength of the grout after 24 h of curing was determined to be 22 MPa. Rubber tapered plugs were used to ensure that the sensor remained in the center and straight into the drilled hole, and to prevent grout leakage. Once grouted, the specimens were allowed to cure at room temperature for at least 1–2 d before testing, ensuring that the grout reached a sufficient strength level.

For the rockbolt-supported specimens, fully grouted grade #6 rebars were used. The rebars were obtained from Dywidag Systems International (DSI) and had a diameter of 19 mm, yield strength of 420 MPa (120 kN), and an ultimate tensile strength of 600 MPa (Fig. 7). To measure the deformation along the rockbolts, the rebars were instrumented with fiber sensors prior to grouting in the specimens. Two diametrically opposed grooves, each with dimensions of 3.1 mm × 3.1 mm, were machined along the entire length of the rockbolt, and the fiber sensor was embedded and

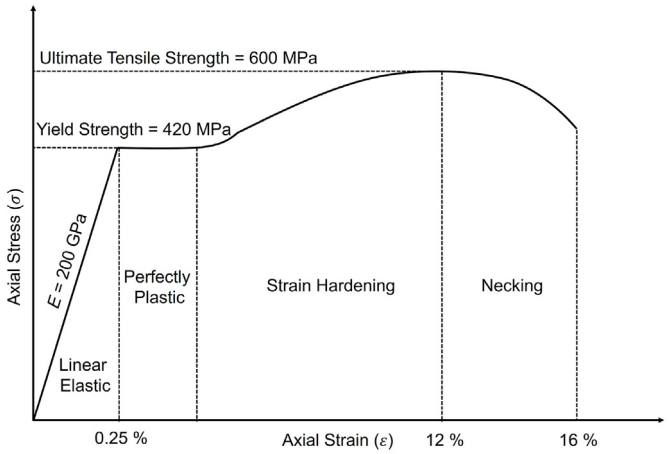

Fig. 7. Representative tensile stress-strain curve of #6 grade 60 rebar (Signer et al., 1997).

encapsulated within the grooves (Fig. 8). The grooves reduced the cross-sectional area by approximately 6.7%, decreasing the yield strength from 120 kN to 112 kN. A single DOS system was utilized for both grooves by looping the sensor at one end, as shown in Fig. 8a. This technique offers redundancy measures and enables the evaluation of the bending-induced strain in the rockbolt. Further information on the development of the fiber optic sensor instrumented rockbolts is described by Hyett et al. (2013) and Forbes et al. (2017).

The instrumented rockbolts were similarly grouted in the specimens as described for the fiber optic sensors installed in the unsupported specimens. The diameter of the drill hole for the rockbolts was 38 mm, leaving approximately 9.5 mm of grout annulus. For the $w/h = 1$ and 2 cases, a single rockbolt without a face plate was installed in the center of the specimens (Fig. 9a). For the $w/h = 0.5$ case, double rockbolts without face plates were installed perpendicular to each other with a distance of 0.35 m between them (Fig. 9b). It should be noted that although two rockbolts were used for $w/h = 0.5$ specimens, only one rockbolt's deformation was monitored due to the availability of only one DOS interrogator system.

To investigate the effect of the wire mesh on the specimens' deformation behavior, galvanized welded wire mesh was used along with the instrumented rockbolt and face plate. The rockbolt was first installed in the specimen, followed by wrapping the wire mesh around the specimen, leaving around 2.5 cm from the top and bottom of the loading face, and connecting it with steel wire ties. The face plate was used with the rockbolts to ensure proper contact of the wire mesh on the specimen's vertical surfaces (Fig. 9c). Table 3 describes the properties of the different support components implemented in this study.

4. Data analysis

4.1. Stress-strain curve adjustment

The axial stress of the test specimens was computed by dividing the total load obtained from the MRS at each loading time step by the cross-sectional area of the specimen (0.25 m^2). The axial strain was calculated by dividing the deformation obtained from the built-in LVDT by the specimen height. It should be noted that the built-in LVDT in the MRS measures the overall deformation between the top and bottom platens, including the load cell, and specimen. This results in a higher strain value than the true specimen strain. Accordingly, the Young's modulus obtained from the linear section of the large-scale laboratory stress-strain curves was low (5.1 GPa) compared to the value obtained from standard UCS tests on cylindrical specimens (10.9 GPa). Sinha et al. (2022) attempted to adjust the strain component by subtracting the load-cell displacement contribution; however, they showed that Young's modulus increased to only 6.1 GPa, which was lower than the value obtained from the UCS tests. This discrepancy was attributed to the stiffness effects of multiple contacts within the platen-specimen-load cell system (Alejano et al., 2020). It is expected that the Young's modulus values should be similar to the standard UCS test (Jackson and Lau, 1990; Darlington et al., 2011) because this rock type does not exhibit a clear size effect (Sinha et al., 2022). Additionally, Young's modulus obtained from the DIC axial stress-strain curve is 10.7 GPa, which is close to the average elastic modulus obtained from the standard UCS tests (10.9 GPa). Therefore, in this study, the strain values were adjusted by dividing

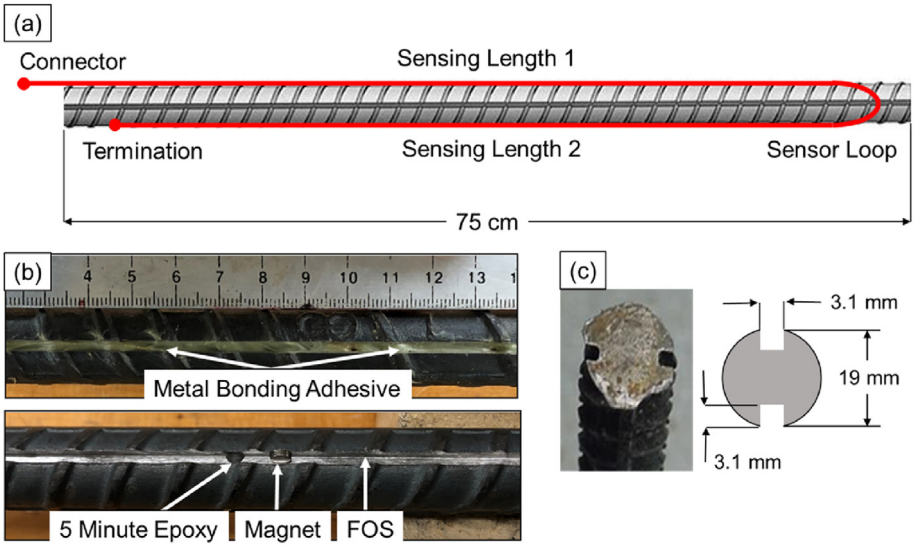

Fig. 8. (a) Fiber optic sensor looped around the rockbolt within machined grooves, (b) Metal bonding adhesive and epoxy have been used to couple the DOS and rockbolt, and (c) Grooves were machined 180° apart to loop the sensors (after Forbes, 2020).

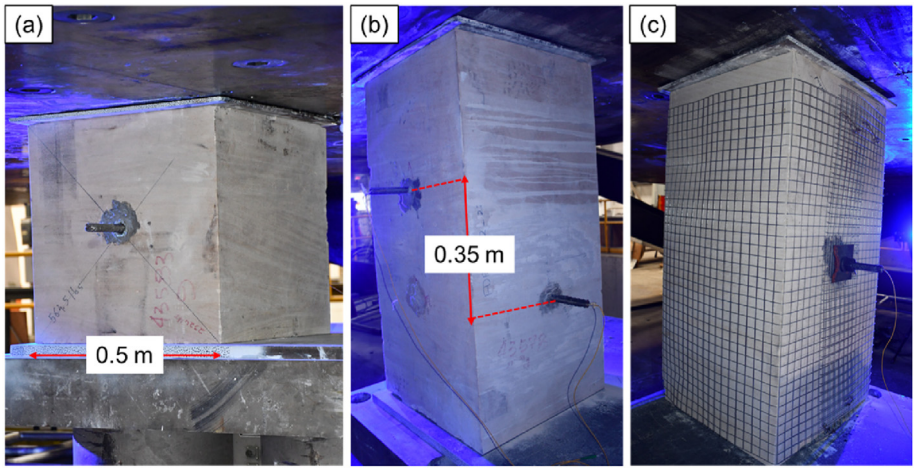

Fig. 9. (a) Single instrumented rockbolt grouted in the center of $w/h = 1$ specimens, (b) Double rockbolt grouted perpendicular to each other in a $w/h = 0.5$ specimens, and (c) Welded wire mesh wrapped around the specimen along with instrumented rockbolt and face plate in $w/h = 0.5$ specimens.

Table 3
Properties summarized for different support components.

Support components	Parameters	Values
Rockbolt	Type	#6 grade 60 rebar
	Diameter	19.05 mm
	Length	75 cm
	Minimum Yield	120 KN
	Manufacturer	DSI
Face Plate	Type	Flat
	Cross-section	4" × 4"
	Thickness	1/4"
	Hole Diameter	7/8"
	Manufacturer	Jennmar
Galvanized Steel Wire Mesh	Type	Welded mesh
	Mesh Size	1" × 1"
	Wire Diameter	0.063"
	Opening Size	0.937"
	Vendor	Home Depot
Grout	Type	Non-shrink precision
	Consistency	Fluid
	Strength after 1 day	22 MPa
	Strength after 3 days	34.5 MPa
	Manufacturer	Quikrete

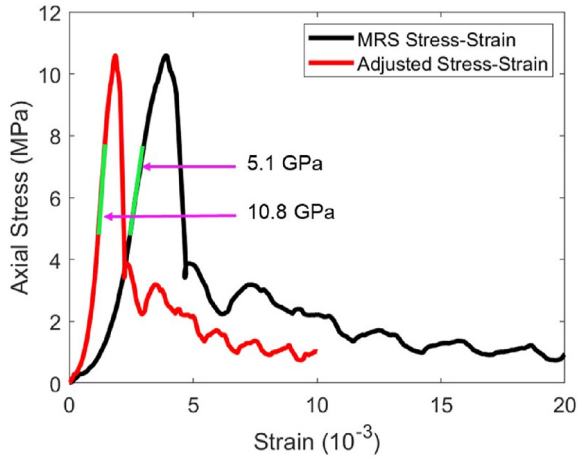

Fig. 10. The Axial stress-strain curve obtained from MRS load-displacement data as well as the adjusted stress-strain curve for a $w/h = 0.5$ specimen (Specimen ID: U_0.5_1), where green segment shows the area where Young's modulus was computed.

the strain value at each load step by a constant factor (variable by test), to obtain a final adjusted stress-strain curve that provided Young's modulus of 10.8 GPa, as shown in Fig. 10.

It should be noted that the adjusted strains are likely to be more accurate only in the elastic region because the actual appropriate adjustment factor is not expected to be constant throughout the test. This is due to the expectation that the relative compliance of the specimen and the rest of the system components changes throughout the test as the specimen accumulates damage. No reliable means for computing a variable adjustment factor was identified, and therefore this is considered beyond the scope of the current study. Nevertheless, the stress-strain curves were adjusted for all w/h ratio specimens to permit comparison of stress-strain behavior for different w/h specimens. Due to the issues in calculating the true strain of the specimens, the remainder of this study is mainly focused on the stress of the limestone specimens (i.e. strength) rather than strain.

4.2. Evaluation of damage thresholds

CI and CD are considered inherent material properties (Martin and Chandler, 1994) and are treated as the lower and upper in situ strength bounds for rocks, respectively (Diederichs, 2003). CI corresponds to the onset of non-linearity in the axial stress-lateral strain curve and can be determined as the point of crack volumetric strain reversal. CD corresponds to the start of non-linearity in the axial stress-axial strain curve under uniaxial loading (Cai et al., 2004; Hoek and Martin, 2014; Walton et al., 2017) and can be estimated from the axial stress-volumetric strain curve under unconfined conditions (Martin, 1997; Diederichs, 2003). Other methods to evaluate CI and CD include acoustic emission (Eberhardt et al., 1998; Ghazvinian, 2010; Zhao et al., 2013) and ultrasonic monitoring (Modiriasari et al., 2017; Shirole et al., 2019).

The lateral strain (both in-plane and out-of-plane) was not measured using direct-contact instrumentation in this study. While the in-plane lateral strain on one surface was assessed using 3D-DIC data, it does not accurately represent the true lateral strain for the cuboidal specimen (reliable out-of-plane strain estimates could not be obtained from the collected data). Therefore, CI was not evaluated. However, previous testing on the same rock type suggested a CI of approximately 35%–45% of the peak strength (Sinha et al., 2022). Accordingly, the CI was estimated as 40% of the peak

strength for all the specimens in this study.

This study used the tangent modulus method to identify the non-linearity in the axial stress-strain curve to identify CD from laboratory data (Diederichs, 2007; Ghazvinian et al., 2012). The tangent modulus is calculated as follows:

$$\text{Tangent Modulus } (\Delta E) = \frac{\Delta\sigma}{\Delta\varepsilon} \tag{1}$$

$$\Delta\sigma = \sigma_{i+6} - \sigma_i \tag{2}$$

$$\Delta\varepsilon = \varepsilon_{i+6} - \varepsilon_i \tag{3}$$

where $\boldsymbol{\sigma}$ is the axial stress, and $\boldsymbol{\varepsilon}$ is the axial strain. The specific length of the difference (i.e. i+6) can be varied to reduce noise in the data. In this study, the tangent modulus was evaluated with a difference in length of six. The tangent modulus was then plotted against the mean value of the stress calculated for the difference in length. CD was interpreted as the first point of monotonic decrease in the tangent modulus. Fig. 11 illustrates the variation in the tangent modulus with mean axial stress for a $w/h = 0.5$ specimen, with the interpreted CD value shown. Similarly, CD was evaluated for all w/h ratio specimens.

4.3. 3D-DIC image processing

The GOM Correlate Professional software was used to analyze the images and evaluate axial (in y-direction) and lateral (in x-direction) surficial deformations. Two essential parameters, facet size and point distance, were used to process and correlate the images to accurately extract surficial displacement/strain. The facet size determines the size of subsets to be compared in the deformed and reference images using statistical criteria, whereas the point distance determines the distance between the centers of neighboring facets. Typically, the point distance is chosen to be smaller than the facet size to ensure overlap between neighboring facets, which improves the accuracy of the results. If the facet size is larger, a longer computation time is required with a poor acquisition of local effects within the facet (averaged over a larger window), whereas if the point distance is smaller, longer computation is required with a high measurement of point density. The facet size was selected to be 32 pixels such that each facet contains at least 3–4 speckle dots. The point distance was maintained at 3/4 of the facet size to ensure a good overlap (GOM, 2019).

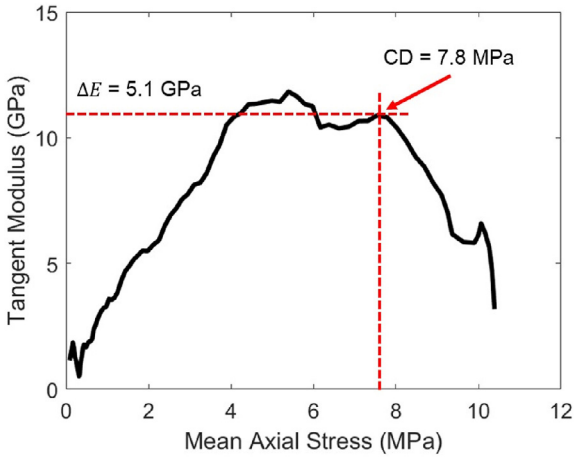

Fig. 11. Plot of tangent modulus with mean axial stress for a $w/h = 0.5$ specimen (Specimen ID: U_0.5_1) to evaluate CD.

4.4. Rockbolt DOS data analysis

During the compression tests, the instrumented rockbolts experienced both axial and bending moment-induced strains. The axial strain was a result of lateral opening and propagation of fractures across the rockbolt. Bending moment-induced strains were due to localized shear movement of the fractures. The strain measured by the DOS can be determined by Eqs. (4) and (5) (Forbes et al., 2017):

$$\varepsilon_T = \varepsilon_{\text{axial}} \pm \varepsilon_{\text{bending}} \tag{4}$$

$$\varepsilon_T = \frac{F}{EA} \pm \frac{Mz}{EI} \tag{5}$$

where $\varepsilon_{\text{axial}}$ is the axial strain in the rockbolt, $\varepsilon_{\text{bending}}$ is the bending strain in the rockbolt??, F is the axial load of the rockbolt, E is Young's modulus of rockbolt, A is the cross-section area of the rockbolt, M is the bending moment, I is the second moment of inertia, and z is the radial distance of the fiber optic sensor from the bolt's neutral axis. In the case of fiber sensors without a loop, only the total strain along the sensors can be measured, and it is not possible to isolate axial and bending strains. However, when using instrumented rockbolts with sensors looped around the bolt length 180° apart, both axial and bending moment-induced strains can be evaluated using the Eqs. (6)–(8):

$$\varepsilon_{\text{axial}} = \frac{\varepsilon_{\text{SL1}} + \varepsilon_{\text{SL2}}}{2} \tag{6}$$

$$\varepsilon_{\text{bendingL1}} = \varepsilon_{\text{SL1}} - \varepsilon_{\text{axial}} \tag{7}$$

$$\varepsilon_{\text{bendingL2}} = \varepsilon_{\text{SL2}} - \varepsilon_{\text{axial}} \tag{8}$$

where ε_{SL1} is the total strain in sensor loop 1, $\varepsilon_{\text{bendingL1}}$ is the bending strain in the sensor loop 1. It should be noted that bending strain is only determined in plane with the two fiber sensing lengths, which may not align with the plane of maximum bending moment. Maximum bending strain can be determined with the addition of an additional fiber optic sensing length (Forbes et al., 2017), but this was investigated by the study.

The axial load along the rockbolts can be evaluated using Hooke's law for the deformation in the elastic range, which is approximately 0.2%–0.25% (2000–2500 micro-strain) for the considered rebar steel. In the elastic region, 1 kN of rockbolt load for 19 mm bolt diameter corresponds to approximately 20×10^{-6}.

5. Unsupported and supported test results results

5.1. Stress-strain curves

Fig. 12 compares the adjusted axial stress-strain curves for specimens with w/h ratios of 0.5, 1, and 2, both with and without installed support. To simplify visualization, only a single representative curve from each test has been displayed. The initial non-linear segment is attributed to the seating of the platens on the loading faces, as well as the crack closure phase of rock deformation. Brittle failure was observed in the post-peak regime, with a sudden drop in strength after the peak for w/h ratios of 0.5 and 1 in unsupported specimens, as is commonly observed in slender rock specimens (Mortazavi et al., 2009; Kaiser et al., 2011; Renani and Martin, 2018). The peak strength and ductility increased with the w/h ratio. This increase can be attributed to the boundary restraint provided by the interface frictional angle, which increases as the $w/$

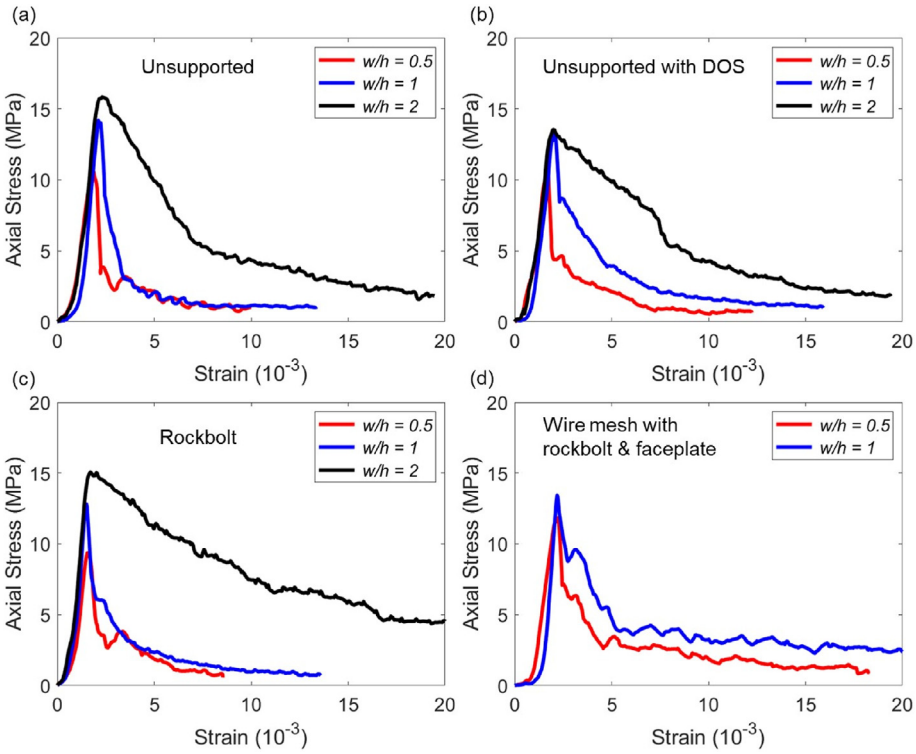

Fig. 12. Representative adjusted axial stress-strain curves for specimens with different *w*/*h* ratios: (a) Unsupported, (b) Unsupported with DOS, (c) Rockbolt supported, and (d) Supported with wire mesh, rockbolt and face plate.

h ratio increases (Dhir and Sangha, 1973; Valiet and Mier, 1996; Diederichs, 2007). The residual strength and ductility increased with the addition of support, particularly in the $w/h = 2$ case.

5.2. Variation of strength parameters

Strength parameters such as the CD threshold, peak strength, and residual strength were evaluated for each tested specimen using the stress-strain curve. Fig. 13 shows the variation in these parameters as a function of *w*/*h* ratio for both the supported and unsupported specimens. Note that the wire mesh support system consists of wire mesh along with rockbolt and faceplate. It was observed that the peak strength did not change substantially depending on the installed support for all *w*/*h* ratios, even when the rockbolt and wire mesh were installed. The normalized CD remained almost constant (approximately 78% of peak strength) for all *w*/*h* ratios for both the supported and unsupported specimens. The residual strength increased as the *w*/*h* ratio increased for both supported and unsupported specimens. With the addition of rockbolts, the residual strength of the $w/h = 0.5$ and 1 specimens did not increase; however, it increased by approximately 2 times for $w/h = 1$ specimens and 1.2 times for $w/h = 0.5$ specimens when wire mesh and rockbolt supported was included. For the $w/h = 2$ case, the residual strength increased around two times just with the addition of a rockbolt.

It should be noted that the wire mesh supported $w/h = 0.5$ and 1 specimens were loaded to substantial deformation in post-peak compared to unsupported and rockbolt-supported specimens. Therefore, it is expected that the residual strength of unsupported and rockbolt supported $w/h = 0.5$ and 1 specimens could be reduced relative to the final recorded stresses under further deformation, meaning the residual strength values presented may be overestimated. However, in these residual strength estimates (taken as the final stress value at the end of the test where the stress-strain curve became approximately flat; see Fig. 12) was taken as a point of comparison between unsupported and supported specimens.

5.3. Failure pattern

The failure pattern of the tested specimens was evaluated using DIC images and pictures taken by the camera after completing the tests. Fig. 14 displays the failure pattern of both unsupported and supported for specimens with $w/h = 0.5$. Two different lateral views (side view 1 and side view 2) are presented for the specimen state after test completion. It is evident that the unsupported specimen exhibits slight spalling accompanied by the formation of a diagonal through-going shear band (Fig. 14a and b). Interestingly, a similar failure pattern was observed even when double rockbolts were used, as shown in Fig. 14c and d. However, in this case, the fracture passed through the rockbolt location along a through-going diagonal shear pathway. On the other hand, when a single rockbolt was used in conjunction with welded wire mesh support, the diagonal fracture still propagated through the rockbolt, but the spalling was contained by the wire mesh (Fig. 14e and f). Consequently, a certain degree of confining stress was generated in the specimen, resulting in a minor increase in the residual strength of $w/h = 0.5$ specimens. The occurrence of failure in the wire mesh, specifically at the corners, tiebacks, and face plate, suggests that the wire mesh was effectively bearing the load.

Fig. 15 illustrates the failure patterns of both unsupported and supported specimens with a *w*/*h* ratio of 1, showcasing different viewpoints of the lateral surface after the test completion. When no support was used for specimens with a *w*/*h* ratio of 1, significant surficial spalling was observed, along with the formation of a conical-shaped cross-shear failure pattern (Fig. 15a and b). The

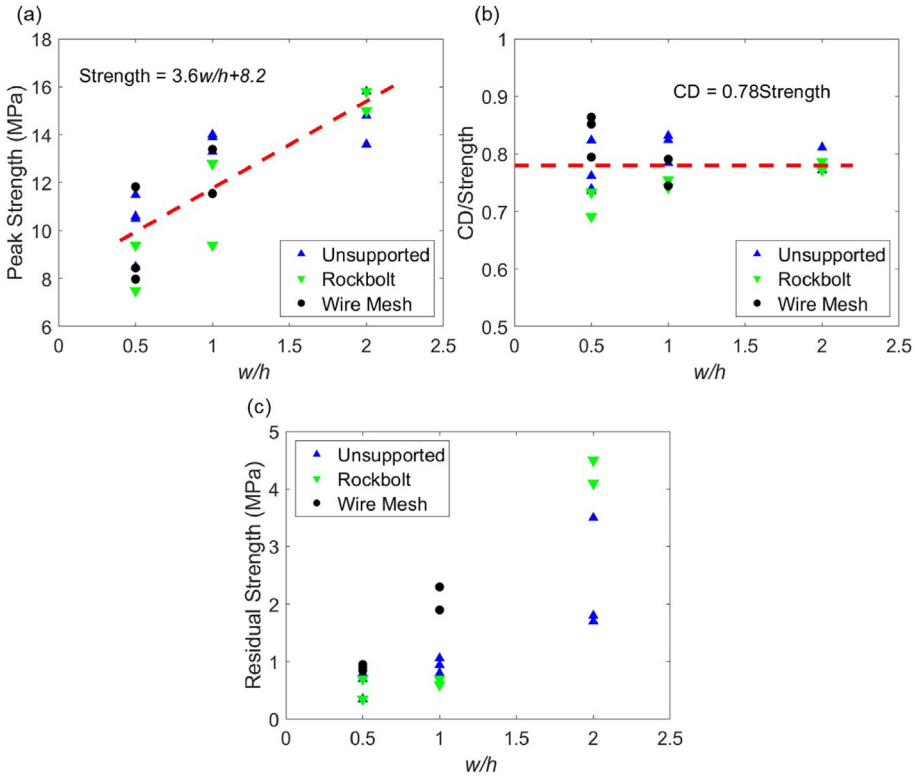

Fig. 13. Variation in strength parameters with w/h ratios for supported and unsupported specimens. The support system in the "Wire Mesh" case consists of welded wire mesh wrapped around the specimen combined with a rockbolt and faceplates: (a) Peak strength, (b) Crack damage, and (c) Residual strength.

supported specimens with a single rockbolt exhibited progressive failure with sidewall spalling. Major spalling occurred from the sides perpendicular to the bolt axis (Fig. 15d), while minor spalling was observed along the bolt axis, leaving a broader intact section (Fig. 15c). Consequently, an increase in the residual strength of the specimens was noted. The behavior of the specimens supported by both wire mesh and a single rockbolt resembled that of the $w/h = 0.5$ specimens, where the failure initiated from the rockbolt location towards the edges of the specimens (Fig. 15e and f). The wire mesh effectively retained the spalled fragments, resulting in an increase in confining stress and residual strength.

Fig. 16 presents the failure patterns of both unsupported and supported specimens with a w/h ratio of 2, from two different lateral surface views once the tests were concluded. For the unsupported specimens, a progressive failure mode was observed, accompanied by significant spalling that resulted in the formation of V-shaped notches from the sides, ultimately shaping the specimens into an hourglass form (Fig. 16a and b). Like $w/h = 1$ case, the installation of a single rockbolt yielded a comparable pattern but with a greater intact width along the bolt axis. However, the amount of spalling was comparatively lower than that in the $w/h = 1$ case, leading to increased confinement in the specimens (Fig. 16c and d).

5.4. 3D-DIC results – evaluation of strain heterogeneity

Both the axial and in-plane lateral strains were computed on the surface of the specimens at each second against the reference image, which was taken before loading, using GOM Correlate Professional software. Here, only one representative result for the unsupported $w/h = 1$ specimen is shown (similar results were obtained for other specimens). The average axial and lateral strains were then evaluated and plotted against the applied axial stress on the specimen, as shown in Fig. 17a. The out-of-plane strain was not computed because there was no base length associated with the Z-direction. Consequently, the estimated volumetric strain ($\varepsilon_{\text{vol.}}$) was approximated using Eq. (9) and is plotted in Fig. 18a. However, we acknowledge that this cannot be considered true volumetric strain and is instead used as a rough approximation to illustrate general trends:

$$\varepsilon_{\text{vol}} = \varepsilon_{yy} + 2\varepsilon_{xx} \tag{9}$$

where ε_{vol} is the volumetric strain, ε_{yy} is the axial strain, and ε_{xx} is the lateral strain. It should also be noted that the speckle pattern on the specimen surfaces begins to break due to spalling in the post-peak region. As a result, the average axial and lateral strains cannot be computed in the post-peak regime; therefore, the strain data are only shown for the pre-peak regime. As shown in Fig. 17a, Young's modulus obtained from the DIC axial stress-strain curve is 10.7 GPa, which is close to the average elastic modulus obtained from the standard UCS tests (10.9 GPa).

The lateral strain is more sensitive to the formation of axial microcracks, which typically start to accelerate around the CI threshold (assumed to be 40% of the peak strength). This acceleration marks the non-linearity in the lateral strain curve. The variation in lateral strain (strain heterogeneity) computed from the DIC at each load step can be represented by the standard deviation (as demonstrated by Shirole et al., 2020; Sinha et al., 2022). Shirole et al. (2020) showed that the heterogeneity in lateral strain starts to accelerate at the CI for low-porosity rocks due to the formation of axial microcracks. However, in the case of Texas Cream limestone, which is highly porous and homogeneous, such behavior was not observed (Sinha et al., 2022).

Fig. 17b presents the standard deviation (SD) of the lateral strain plotted against axial stress. As illustrated, the SD remained constant

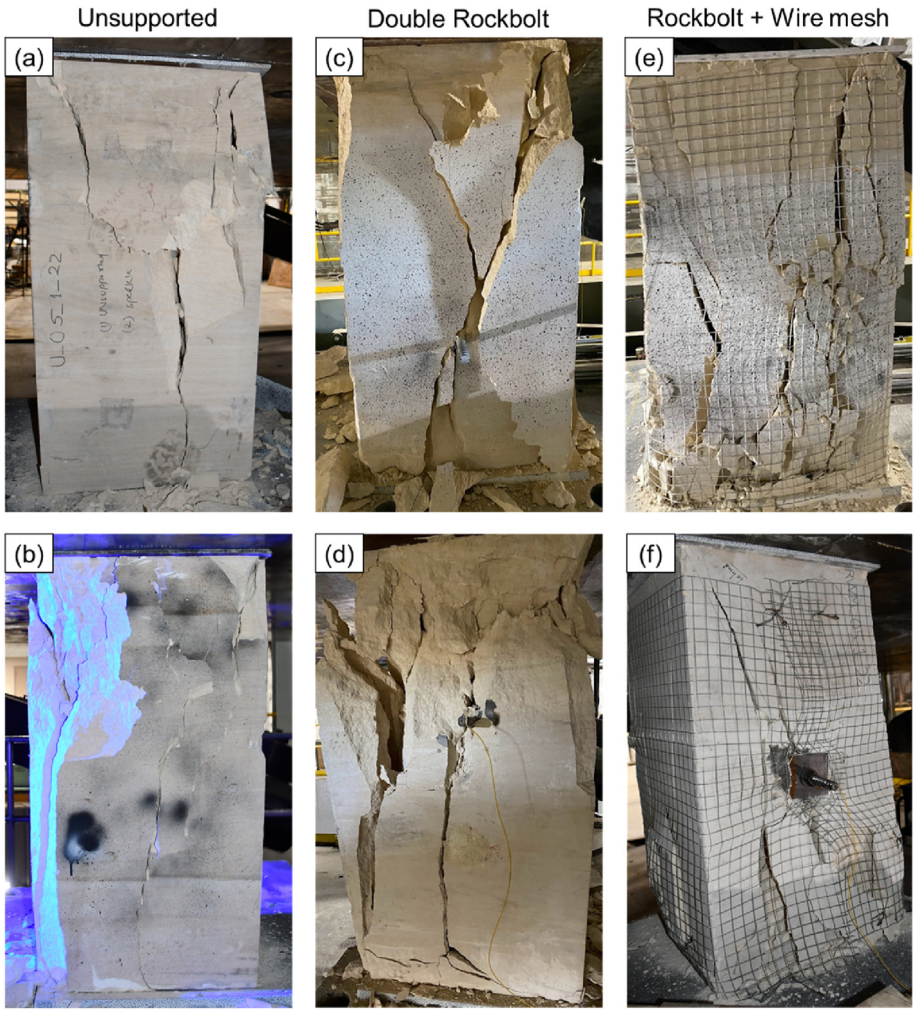

Fig. 14. Failure pattern of $w/h = 0.5$ specimens: (a) Unsupported view 1, (b) Unsupported view 2, (c) Supported with double-bolt view 1, (d) Supported with double-bolt view 2, (e) Supported with welded wire mesh and rockbolt view 1, and (f) Supported with welded wire mesh and rockbolt view 2.

until 80% of the peak strength and started to accelerate thereafter (at an axial stress of 11.2 MPa). Additionally, volumetric strain reversal was observed at the same stress point (Fig. 17a). The CD threshold obtained from the tangent modulus method was approximately 11.6 MPa. This suggests that strain heterogeneity in Texas Cream limestone becomes more pronounced on the surface around the CD threshold, where crack coalescence begins to accelerate. Hence, the acceleration point in the heterogeneity of the lateral strain can be approximated by the CD value for this rock. Fig. 17c displays the point of lateral strain localization (top and bottom) at the CD threshold, eventually coalescing to form the fracture pathway and becoming prominent in the post-peak region (Fig. 17d).

5.5. DOS results for unsupported specimens

In the case of unsupported specimens, the fiber sensors were not looped diametrically around the PVC pipe like the instrumented rockbolts. Hence, the axial and bending strains could not be distinguished. Instead, the value represents the total strain, where a negative value indicates compression, and a positive value indicates tension.

Fig. 18 illustrates the strain profile along the fiber sensor for a specimen with a w/h ratio of 0.5 at three different stress levels (peak strength is 8.5 MPa). The image of the specimen failure was captured after the peak strength point, as no prominent cracks were visible on the surface before reaching peak strength. Relatively small strains were observed in the sensor at 40% of the peak strength (near the CI threshold). At higher stress levels near CD (which is 82% of the peak strength for this specimen), a higher degree of strain starts to accumulate along the sensor. The sensor broke just after the CD threshold, at around 85% of the peak strength, due to the higher localized strain that exceeded the sensor capacity; therefore, data was not captured in the post-peak region. Two peaks in strain were observed in the sensor data (denoted by the vertical black dotted line), representing localized large deformations in the rock due to crack opening and sliding along shear planes. Cracks were also visible at the same location on the specimen surface (points A and B) during the post-peak portion of the test.

For the specimens with $w/h = 2$, a similar evolution of the strain on the sensor with respect to the axial stress level was observed. Fig. 19 presents the strain profile along the sensor for one specimen with $w/h = 2$. The sensor started accumulating strain around CI (40% of the peak strength), but the strain accumulation accelerated around CD (81% of the peak strength for this specimen). The sensor incurred damage at approximately 95% of the peak strength due to highly localized strain accumulation; consequently, data beyond

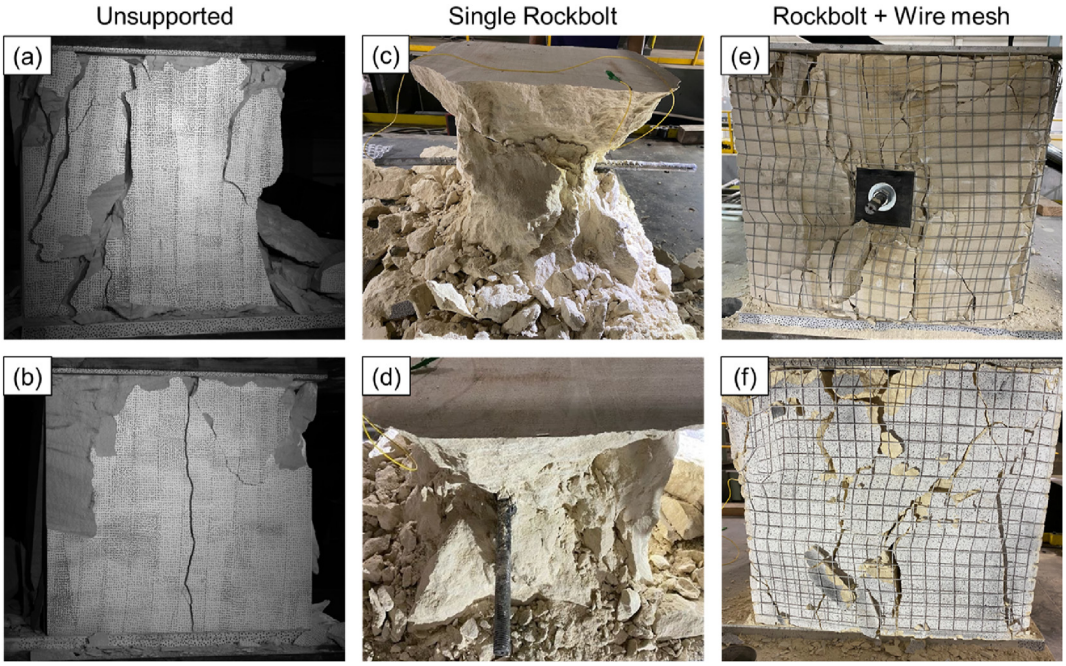

Fig. 15. Failure pattern of specimens with $w/h = 1$: (a) Unsupported view 1, (b) Unsupported view 2, (c) Supported with single bolt view 1, (d) Supported with single bolt view 2, (e) Supported with welded wire mesh and rockbolt view 1, and (f) Supported with welded wire mesh and rockbolt view 2.

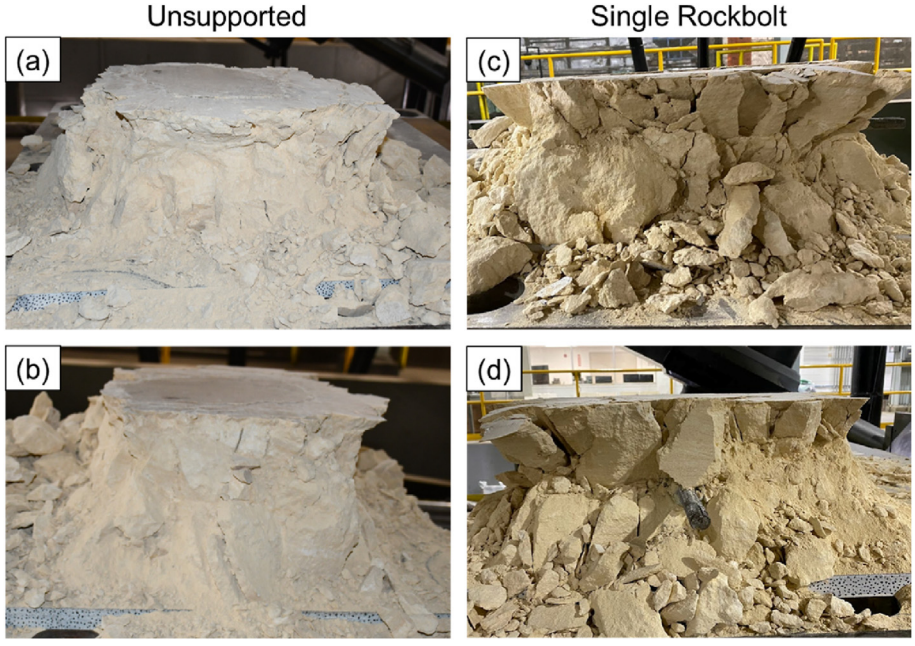

Fig. 16. Failure pattern of specimens with $w/h = 2$: (a) Unsupported view 1, (b) Unsupported view 2, (c) Supported with single bolt view 1, and (d) Supported with single bolt view 2.

that point could not be obtained. Notably, the strain data exhibited multiple spikes, unlike the $w/h = 0.5$ which had only two spikes. This difference was attributed to the failure mechanism of the specimens with $w/h = 2$, where multiple vertical cracks formed from top to bottom throughout the specimen.

As discussed earlier, the axial and lateral strains on the specimen surface can be obtained using the 3D-DIC system, and the heterogeneity of the strain can be represented by evaluating the standard deviation in the lateral strain data. Similarly, the heterogeneity of the fiber strain data for the unsupported specimens was calculated using the standard deviation along the fiber sensor's length for each time step corresponding to the load applied during the compression tests. No definitive correlation was established between the heterogeneity in the DOS-instrumented rockbolt strain data and the CD threshold; accordingly, the heterogeneity in the rockbolt strain data is not presented. Nonetheless, a qualitative correlation was observed between the rockbolt strain profile and the fracture location on the specimen surface (as observed in images obtained

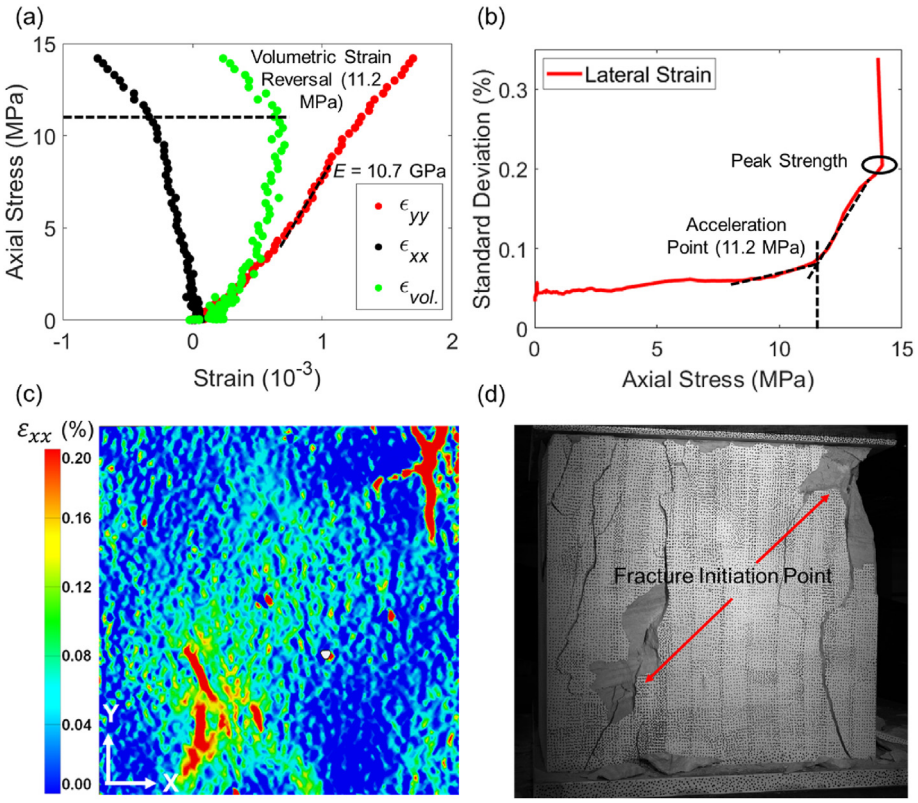

Fig. 17. The plots are generated for an unsupported specimen with a *w*/*h* ratio of 1 (Specimen ID: U_1_1): (a) Axial, lateral, and volumetric strains obtained from DIC plotted against axial stress, (b) Standard deviation plot of lateral strain to identify the surficial strain heterogeneity, (c) Contour of lateral strain at a vertical stress of 11.2 MPa, and (d) Fracture formation on the specimen in the post-peak region, originating from the localized zone at CD.

through 3D-DIC) and is discussed in Section 5.6.

Fig. 20a shows the lateral strain data heterogeneity obtained from 3D-DIC, while Fig. 20b illustrates the fiber sensor strain data heterogeneity for a $w/h = 1$ specimen (Specimen ID: UF_1_2). The heterogeneity in lateral strain on the surface, obtained through DIC, starts accelerating at a stress level of 11.3 MPa, close to the CD threshold of 1 MPa, determined using the tangent modulus method for the same specimen (Fig. 20c). A similar trend was observed in the DOS strain data, where the acceleration of strain heterogeneity occurred at approximately 11.6 MPa, near the CD value (Fig. 20b). At CD (1 MPa), which marks the onset of formation of macroscopic cracks, strain localization in the lateral strain data on the surface can also be observed (Fig. 20d). This implies a correlation between surficial rock deformation (strain localization and heterogeneity), volumetric deformation (represented by DOS data), and the overall development of macroscopic cracks (post-CD). This further affirms that the DOS data accurately represent rockmass deformation.

5.6. DOS Results for supported specimens

This section discusses the rockbolt deformation characteristics in the pre-peak and post-peak regions of the stress-strain curve. Fig. 21a illustrates the total strain on the sensor for loops 1 (SL1) and 2 (SL2) along the rockbolt length, for a representative $w/h = 1$ specimen. Both axial and bending strains were computed using Eqs. (7)–(9), and are presented in Fig. 21b and c, respectively. The bending strain in sensor loop 1 (SL1) and sensor loop 2 (SL1) have the same magnitude but opposite signs; hence, only the absolute value can be shown to represent the bending strain. The axial load corresponding to each axial strain data point was computed and plotted along the rockbolt length (Fig. 21d). Similarly, the axial and bending strains were computed in the rockbolt for all the supported specimens.

The actual magnitude and orientation of the bending moment in the rockbolts depend on the alignment of the sensor axis with respect to the deformation or applied load. When the sensors are oriented parallel to the applied load, the bending strain indicates that the rockbolt is bent within the plane of the applied load. However, if the sensor orientation is different, the rockbolt can experience bending out of the plane of the applied load. This bending can either be hogging or sagging, depending on the deformation of SL1 and SL2. Therefore, Fig. 21b only allows us to identify the location of the bending moments in the bolt; the actual alignment depends on the sensor's orientation, which varies from one specimen to another in this study. This shortcoming can be overcome by coupling a three-sensor loop oriented 120° apart diametrically (Forbes et al., 2017).

5.6.1. Rockbolt deformation without face plate

The rockbolts underwent both axial and bending deformation during the compression tests, and the respective strain components were computed using the DOS data. Fig. 22 illustrates the axial and bending strain profiles for the rockbolt-supported specimens at the CI, CD, and peak strength for all considered *w*/*h* ratios. Multiple tests were conducted for each *w*/*h* ratio supported with rockbolts, but only one representative data point for each *w*/*h* ratio is presented here. Although the spatial resolution of the fiber sensors was 0.65 mm, a moving average was applied at an interval of 15 to reduce noise, resulting in an effective spatial resolution of 1 cm for strain evaluation.

As observed, a substantial axial strain began to develop in the rockbolts either at or after reaching the CD threshold for all *w*/*h*

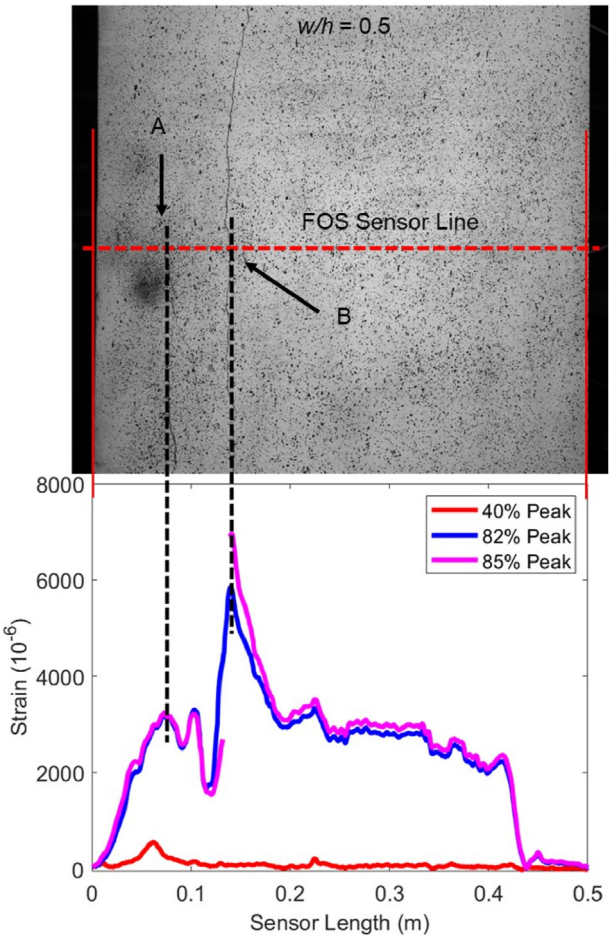

Fig. 18. The strain profile along sensor length for a $w/h = 0.5$ specimen which was grouted in the center of the specimen (Specimen ID: UF_0.5_2), at three different stress levels. The peak strength of the specimen is 8.5 MPa and the specimen image shown was captured in the post-peak region of the stress-strain curve (at 87% of the peak).

ratios. Before this threshold was reached, small amounts of axial strain were observed, accompanied by negligible bending strain. After surpassing the CD threshold, both axial and bending strains accumulated in the rockbolts, with the former becoming more prominent until reaching the peak strength. However, it was noted that the bending strain in the $w/h = 1$ specimen was lower than the $w/h = 0.5$ and 2 specimens at the peak strength. Since the bending strain is interpreted to be influenced by the localized shear fracture, we didn't observe any shear cracks across the rockbolt length at the peak strength for $w/h = 1$ specimen as compared to $w/h = 0.5$ and 2 specimens. At the peak strengths of the respective w/h ratios, the axial strain increased with the w/h ratio. Additionally, the strain profile displayed multiple spikes for $w/h = 2$ compared to $w/h = 1$ and 0.5.

Figs. 23–25 illustrate the axial and bending strain profiles of the rockbolt for all three w/h ratios in the post-peak region, alongside images taken from DIC at the same stress level. These plots correspond to the w/h ratio specimens shown in Fig. 22. The localized peaks in the axial and bending strains within the rockbolts suggest the presence of localized extensional strain (caused by the lateral opening of cracks) and localized shear zones in the center of the specimens, respectively. The fiber sensor on the rockbolt for a w/h ratio of 2 sustained damage during the post-peak phase, occurring after 90% of the peak strength. This damage resulted from the significant deformation of the bolt; consequently, the data beyond

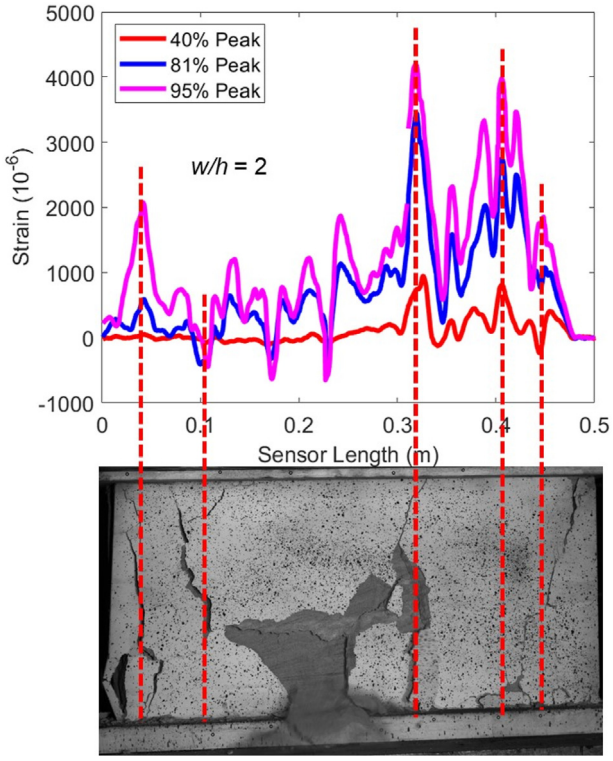

Fig. 19. The strain profile along sensor length for a $w/h = 2$ specimen which was grouted in the center of the specimen (Specimen ID: UF_2_2), at three different stress levels. The peak strength of the specimen is 14.9 MPa and the specimen image shown was captured in the post-peak region of the stress-strain curve (at 80% of the peak).

that point were not included.

For specimens with w/h ratios of 0.5 and 1, only a few localized peaks in axial and bending strain were observed, in contrast to multiple spikes seen in the case of $w/h = 2$. This discrepancy can be attributed to the different failure mechanisms in slender and squatter specimens (as discussed in Section 5.3). In the case of $w/h = 2$, the failure mechanism involved progressive spalling, resulting in significant fracturing along the specimen periphery and the formation of multiple localized damage zones (Fig. 25). The magnitudes of axial and bending strains in the rockbolts increased with increasing w/h ratio, indicating greater rockbolt load mobilization in squatter specimens ($w/h = 2$). Consequently, the residual strength of the single rockbolt-supported $w/h = 2$ specimens was nearly double that of the unsupported specimens. However, the residual strength remained unchanged with the addition of rockbolts for specimens with $w/h = 1$ and 0.5.

In the case of specimens with $w/h = 1$ and 0.5, the maximum axial strain in the rockbolt was below 1000 x 10^{-6} strain, indicating that the bolt load was less than 50 kN (approximately 40% of the yield limit). In contrast, for $w/h = 2$ specimens, the axial strain in the rockbolt exceeded 2500 x 10^{-6} (the yield strain) at multiple locations (see Fig. 25). This suggests that the rockbolt element yielded and underwent plastic deformation either within its perfectly plastic region or strain-hardening region (Fig. 7). However, inspection of the rockbolt after completing the test revealed that the rockbolt did not rupture. Therefore, it can be concluded that the total accumulated axial strain remained below the rupture limit 16%).

5.6.2. Rockbolt with wire mesh and face plates

Fig. 26 displays the axial and bending strain profiles along the

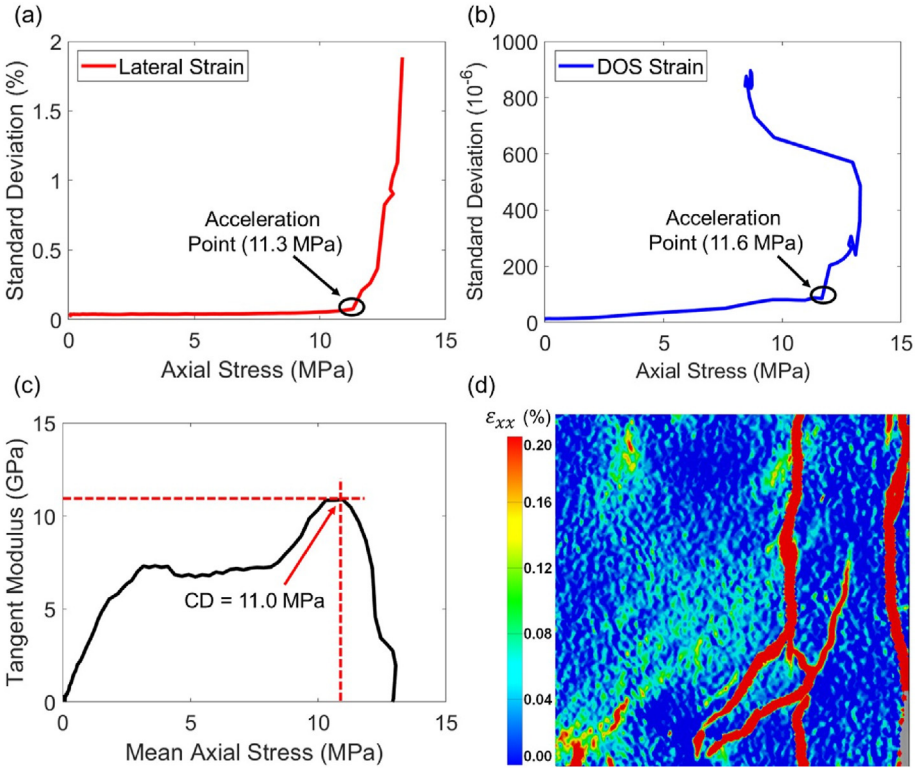

Fig. 20. All plots are presented for a representative unsupported $w/h = 1$ specimen grouted with DOS (Specimen ID: UF_1_2, peak strength is 13.3 MPa): (a) Lateral strain heterogeneity obtained from 3D-DIC on one surface, (b) Strain heterogeneity in the DOS data, (c) CD evaluation using the Tangent Modulus method, and (d) Surface lateral strain localization at CD (1 MPA).

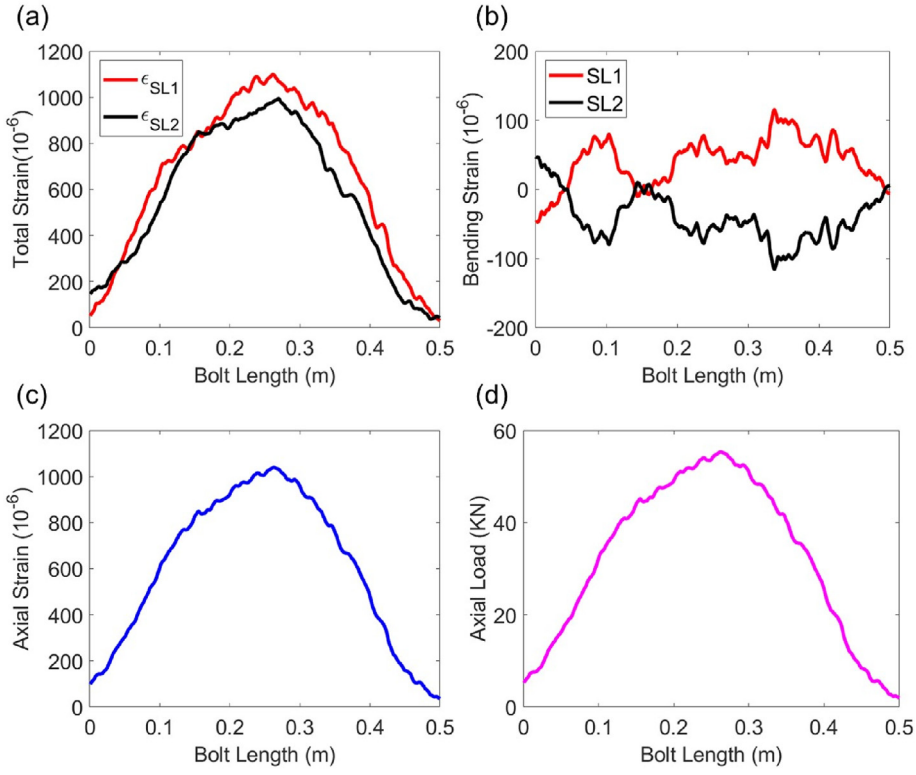

Fig. 21. All plots are shown for a representative $w/h = 1$ specimen at 7.6 MPa in the post-peak region of stress-strain curve (Specimen ID: R_1_2 and peak strength is 9.4 MPa): (a) Total strain obtained along the rockbolt fiber sensor in loops 1 (SL1) and 2 (SL2), (b) Bending strain profile along the bolt length in loops 1 (SL1) and 2 (SL2), (c) Axial strain profile along the bolt length, and (d) Axial load profile obtained through Hooke's law.

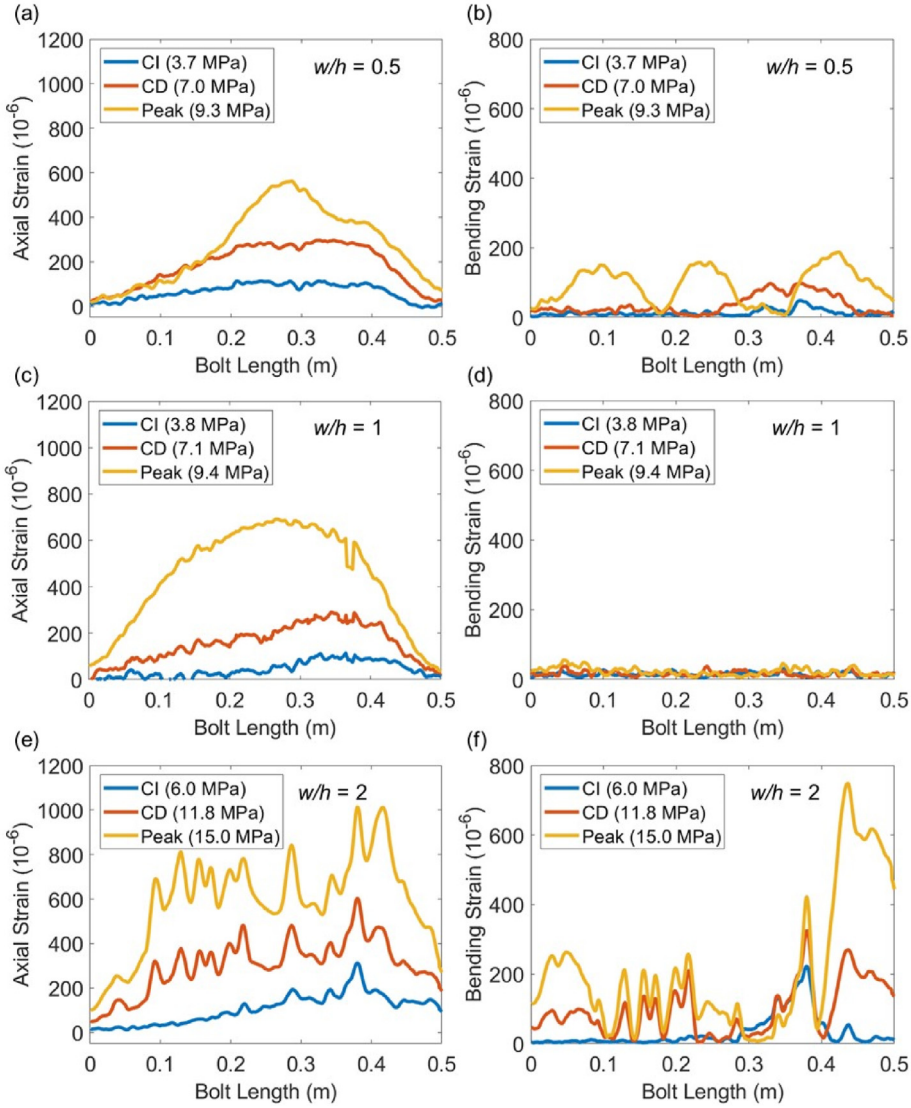

Fig. 22. Representative axial and bending strain profiles of the rockbolt obtained at different *w*/*h* ratios corresponding to their respective CI, CD, and peak strength. The profiles are shown for the following Specimen IDs: (a, b) Specimen ID: DR_0.5_2, (c, d) Specimen ID: R_1_2, and (e, f) Specimen ID: R_2_2.

length of the rockbolt at CI, CD, and peak strength for w/h ratios of 0.5 and 1 wire mesh supported specimens. Only one representative scenario for $w/h = 0.5$ and 1 specimens are presented here. No tests were conducted for $w/h = 2$ with the rockbolt supported by wire mesh and face plates; this scenario will be considered for future testing.

The strain profile trend resembled that of specimens supported solely by the rockbolt, wherein significant strain accumulation occurred in the rockbolt after the CD threshold. However, both the axial and bending strains in the rockbolt after reaching CD were higher than those in the rockbolt without a face plate and wire mesh. This suggests that the combination of wire mesh and face plates held spalled material in place, resulting in increased confinement around the specimen. Consequently, the specimens were able to undergo significant axial and lateral inelastic deformation in a stable manner, leading to increased rockbolt deformation and load mobilization.

In the post-peak regime, the axial and bending strains in the rockbolt for $w/h = 1$ specimens were higher than those for $w/h = 0.5$ specimens, implying that the wire mesh combined with a single rockbolt provided more effective confinement for the wider specimens than the slender ones (Fig. 27). Consequently, a significant increase in residual strength was observed for $w/h = 1$ specimens (from 1.1 MPa to 2.3 MPa) compared to $w/h = 0.5$ specimens when using a rockbolt with wire mesh and face plates. This is because although the surface support prevented spalling and degradation of the specimens in both cases, it didn't inhibit the development of the shear failure mechanism in $w/h = 0.5$ specimens. Specifically, this mechanism resulted in limited dilatancy along the rockbolt axis, leading to lower rockbolt mobilization. In contrast, for $w/h = 1$ specimens, the failure mechanism shifted towards progressive spalling, inducing relatively more lateral dilatancy and, consequently, greater rockbolt mobilization. This observation is supported by the visible failure of the wire mesh around the edges, which is more pronounced for $w/h = 0.5$ specimens than for $w/h = 1$ specimens (Fig. 28).

Additionally, significant deformation was observed at the ends of the rockbolt where the face plates were installed. The wire mesh directly transferred the load to the faces of the specimen; however, the face plate aided in load mobilization in the rockbolt near the

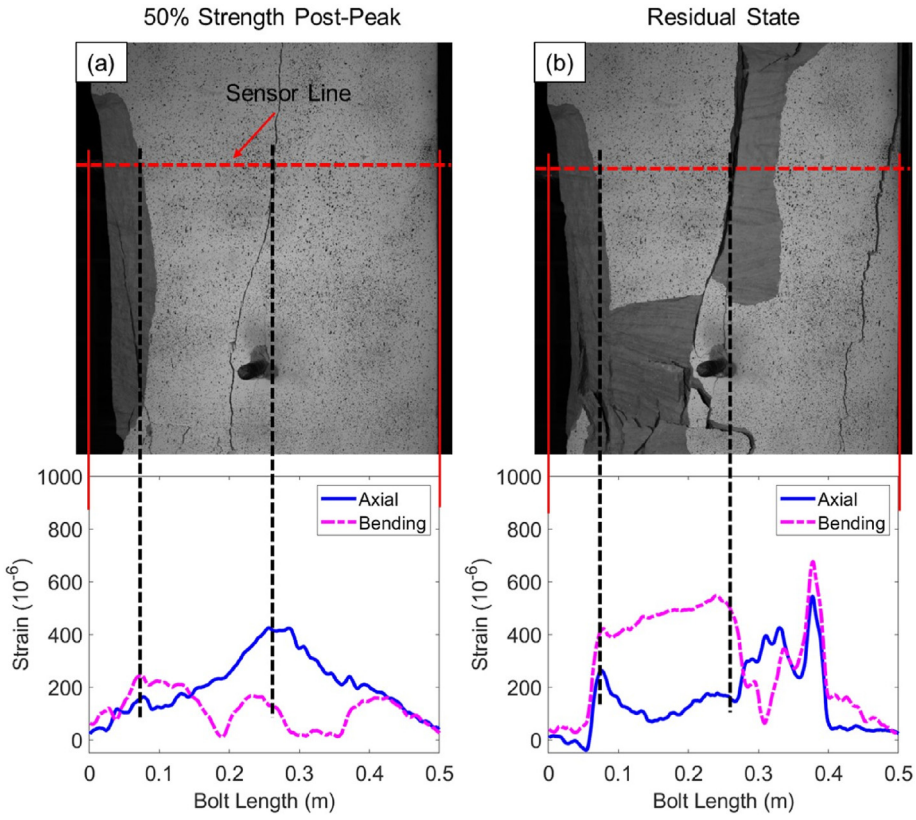

Fig. 23. Axial and bending strain profile in the post-peak region, where black dotted line represents the localized behavior in the rockbolt which can be noticed on the surface for a $w/h = 0.5$ specimen (Specimen ID: DR_0.5_2 and peak strength is 9.3 MPa).

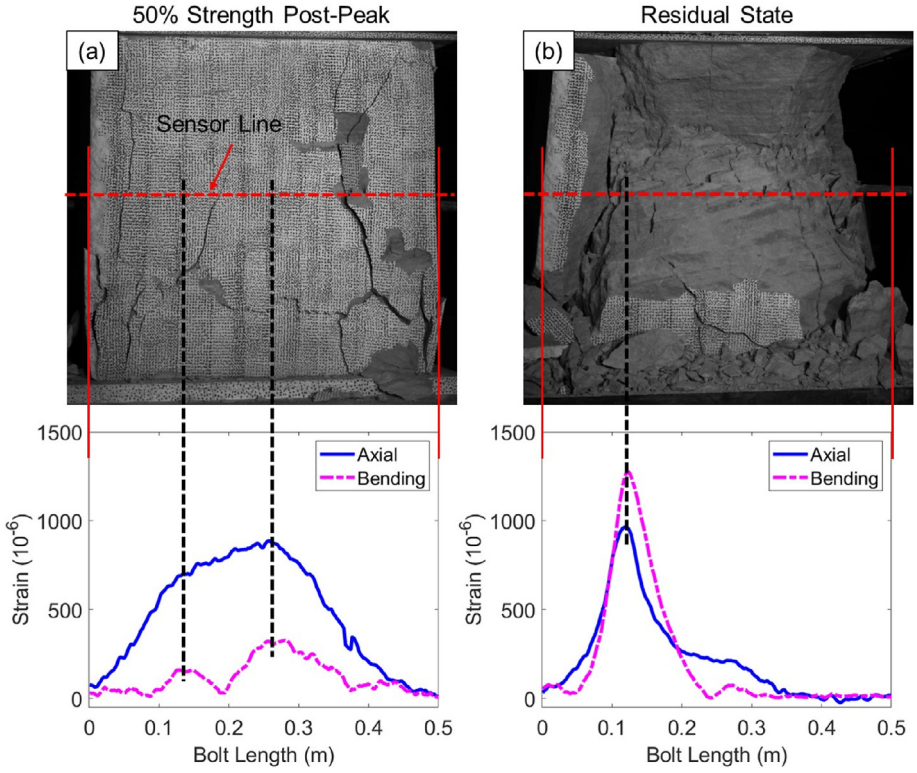

Fig. 24. Axial and bending strain profile in the post-peak region, where black dotted line represents the localized behavior in the rockbolt which can be noticed on the surface for a $w/h = 1$ specimen (Specimen ID: R_1_2 and peak strength is 9.4 MPa).

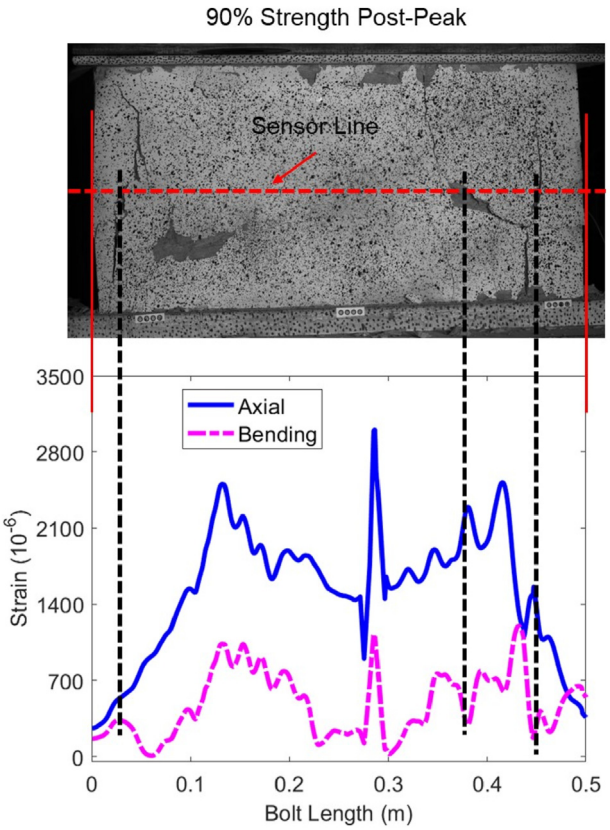

Fig. 25. Axial and bending strain profile in the post-peak region, where the black dotted line represents the localized behavior in the rockbolt which can be noticed on the surface for $w/h = 2$ specimen at 90% post-peak strength (Specimen ID: R_2_2 and peak strength is 15.0 MPa).

specimen faces (which was nearly negligible in specimens without face plates), resulting in higher stress concentration. Consequently, the wire mesh was cut off by the edges of the face plates (Fig. 28). The surface support effectively prevented spalling and degradation of the specimen sides more for specimens with $w/h = 1$ by maintaining a baggage zone of fractured rock (Forbes et al., 2020). This generated confining stress around the specimen periphery, inhibiting crack propagation toward the pillar core and ultimately impeding the progression of pillar damage.

6. Discussion

6.1. Comparison of small-scale and large-scale laboratory strength data

As mentioned previously, small-scale uniaxial compressive tests were conducted at different w/h ratios, with a fixed cross-section of 15 cm × 15 cm. The height varied from 30 cm to 5 cm, resulting in four different w/h ratios (Chaurasia and Walton, 2023). Fig. 29 illustrates a comparison of the peak strength obtained from both small-scale and large-scale laboratory tests on the same rock for the unsupported conditions. The peak strength values from both small-scale and large-scale laboratory tests for w/h ratios of 0.5, 1, and 2 are nearly identical. This observation suggests that, in addition to not exhibiting a size effect on cubic specimens, Texas Cream limestone also shows no size effect on strength for the various w/h ratios considered. A least-squares linear regression model was fit to the combined small-scale and large-scale laboratory peak strength data to obtain linear strength model parameters for the rock in question (Eq. (11)). Note that the strength formula obtained from the current study is highly similar to the empirically derived field-scale linear pillar strength formulae in the literature (Obert and Duvall, 1967; Krauland and Soder, 1987; Sjoberg, 1992). However, Eq. (10) does not have a size effect parameter compared to common field-scale empirical pillar strength formulae, where the compressive strength obtained from the lab test is multiplied by a factor between 0 and 1 to estimate the in-situ rock mass strength:

$$\sigma_p = 12.9(0.212w/h + 0.788) \tag{10}$$

Empirical pillar strength formulae and associated design methods are based solely on the applied load and the peak strength, without explicit consideration of the post-peak load-carrying capacity of pillars. Wagner (1980) observed through in-situ testing that the central core can withstand very high stresses even when the pillar has been compressed beyond its peak strength. He notes that the strength of the core increases with an increase in w/h, and the post-peak behavior becomes more ductile. Similar behavior was observed in both large-scale and small-scale laboratory tests, where the residual strength increases with the w/h ratio (see Fig. 30). However, squatter specimens on the small scale exhibited significantly higher residual strength compared to the large-scale specimens. An outlier was noted for the $w/h = 1$ specimen at the small scale; only one specimen of $w/h = 1$ provided a complete stress–strain curve, and it was weaker than the overall trend implied by the data for the other w/h cases.

We interpret that the variation in residual strength between scales could be attributed to two potential causes. First, the applied loading strain rate was higher in large-scale tests (e.g. $16e^{-5}$/s for the specimen with $w/h = 2$) compared to small-scale tests (e.g. $6.5e^{-5}$/s for the specimen with $w/h = 2$) for each w/h ratio due to the use of two different loading frames with differing control capabilities. At higher strain rates, the specimen has less time to efficiently redistribute the applied stress, leading to non-uniform distribution and an increased propensity for brittle damage localization and lower residual strength (Bhandari and Inoue, 2005). Note that this is contrary to the peak strength effect, where strength tends to increase for higher strain rates, although we note that no apparent strain rate effect on peak strength was observed in our study (Blanton, 1981; Olsson, 1991; Li et al., 1999).

Second, there could be an absolute size effect on the residual strength of the considered rock. Even though the considered rock is homogenous, strain heterogeneity/localization takes place once crack coalesce starts at CD (Sinha et al., 2022). Labuz and Biolzi (2007) showed that once the uniform deformation bifurcates or localizes near the point of peak stress, the overall post-peak response becomes size-dependent (due to heterogeneity of the damage distribution in the specimen). In general, smaller specimens accumulate damage more uniformly in post-peak, leading to higher residual strength, while larger specimens may experience more localized damage.

Even for the large-scale specimens, however, a non-negligible residual strength was noted for the squatter specimens (up to 20% of peak strength for $w/h = 2$). This implies that a relatively squat pillar may contribute to more to global stability than is implied by typical design methods if it exhibits ductility after reaching peak strength. Consequently, the characterization of the post-peak behavior of a pillar and incorporation of this information into the pillar design methodology has the potential to contribute to design optimization.

6.2. Practical implications

This study was not intended to provide support design

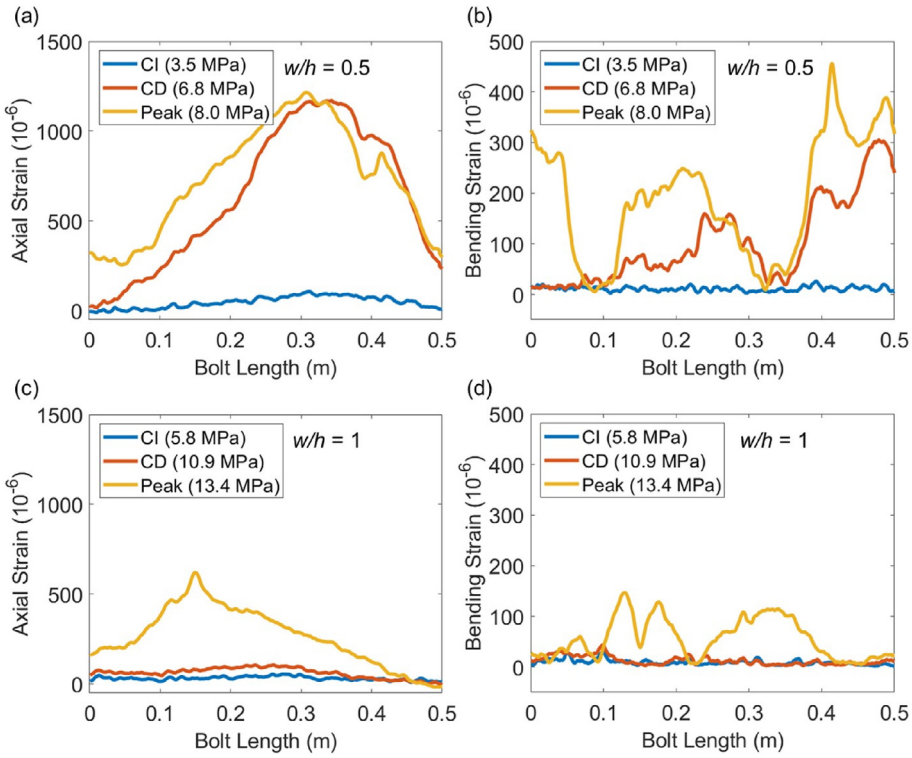

Fig. 26. Axial and bending strain profile of the rockbolts for *w/h* ratio of 0.5 and 1 specimens supported with wire mesh and face plates at their respective CI, CD, and peak strength: (a, b) Specimen ID: WR_0.5_1; (c, d) Specimen ID: RM_1_2.

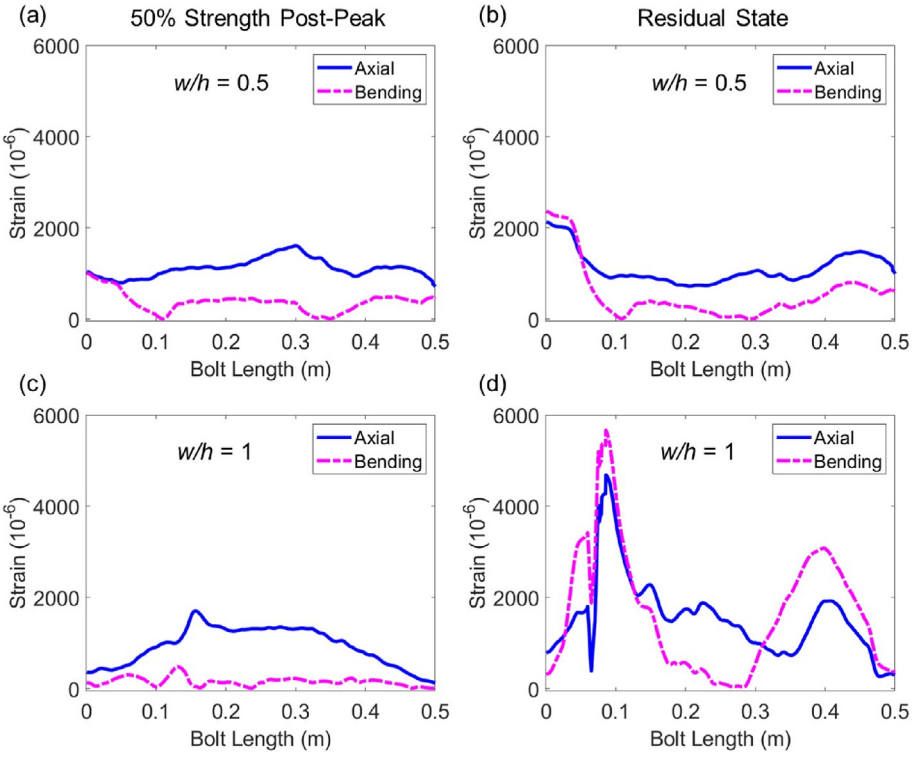

Fig. 27. Axial and bending strains profile along the rockbolt length at two different stress levels in the post-peak region of stress-strain curve for *w/h* = 0.5 and 1 specimens, supported with wire mesh and face plates: (a, b) Specimen ID: WR_0.5_1, and (c, d) Specimen ID: RM_1_2.

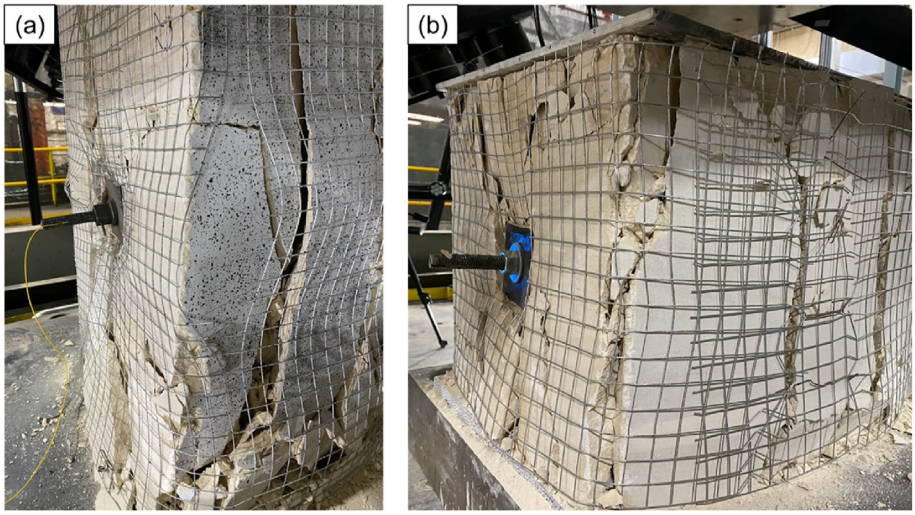

Fig. 28. The failure of the wire mesh at the edges is more prominent in specimens with a *w*/*h* ratio of 0.5 compared to those with a *w*/*h* ratio of 1: (a) Specimen ID: WR_0.5_1, and (b) Specimen ID: WR_1_2.

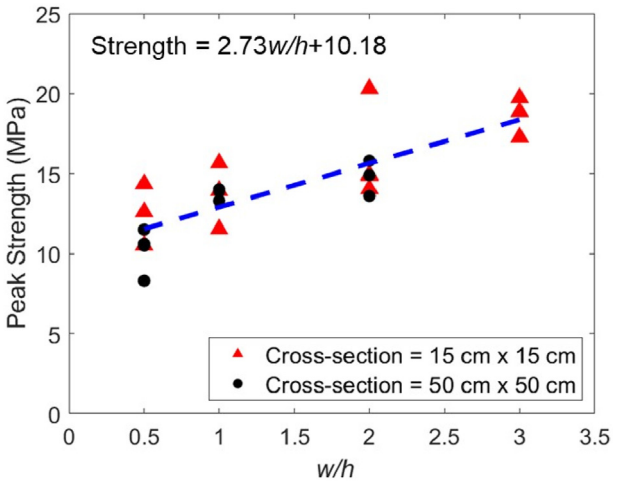

Fig. 29. Comparison of peak strength of large-scale and small-scale uniaxial compressive tests at different *w*/*h* ratios.

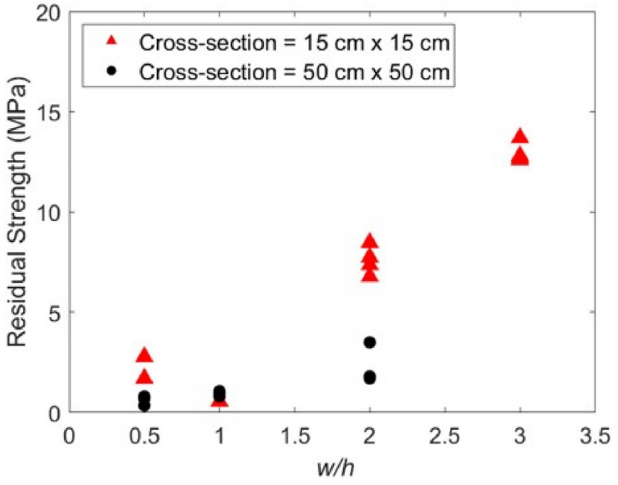

Fig. 30. Comparison of residual strength of large-scale and small-scale uniaxial compressive tests at different *w*/*h* ratios.

guidelines for pillars, given the limited number of conditions that were feasible to evaluate at the selected testing scale. Rather, the primary objective of this study was to evaluate the pillar-support interaction at different *w*/*h* ratios both in terms of support effects on overall pillar stress-strain behavior as well as support characteristics. Large-scale laboratory tests enabled the installation of full-scale support elements, allowing for more direct extrapolation of results to in-situ pillars than is typically possible.

The use of high spatial resolution fiber optic sensors enabled the characterization of rockbolt deformation at a sub-mm level. This offers advantages relative to previous studies that have used a limited number of strain gauges at discrete locations (greater than 10 cm distance apart) to evaluate the load and deformation characteristics of rockbolts and cable bolts (e.g. Signer et al., 1997; Kostecki, 2013), where localized displacement and fracturing could be missed if they occur between the strain gauges (Forbes et al., 2018). Moreover, with the two-groove geometric configuration of the sensor, both axial and bending deformation of the rockbolt were computed. This enabled the identification of the specimen's deformation behavior at the small-scale, where axial strain of the rockbolt implies extensional crack growth, and bending strain implies localized shear fracture (Li and Stillborg, 1999).

At the scale of the full pillar, we found that the installed rock support does not influence the peak strength of the pillars for the considered *w*/*h* ratios; thus, such support cannot increase the factor of safety as considered in traditional designs. This behavior is due to the passive nature of the applied support elements, which begin to provide confinement once inelastic strain starts accumulating in the specimen (typically around the point of peak strength). A similar observation was made by Alejano et al. (2017), who concluded that a cable strap surrounding small-scale rock specimens (for $w/h = 0.5$) does not influence their peak strength but does increase the residual strength. Sinha and Walton (2021) also reported a comparable response for a granite pillar model with $w/h = 1$ in UDEC, even with the installation of 10 rockbolts. However, they noted an increase in peak strength for $w/h = 2$ and 3 models when the support density was increased. This behavior was attributed to a larger amount of pre-peak inelastic damage in the model after the CD threshold in higher *w*/*h* ratios, further mobilizing the rockbolt load. Hence, there is a potential for increased strength at higher *w*/*h* ratios with an increase in support density and/or pre-peak specimen dilatancy that mobilizes rockbolt

resistance. However, our data does not demonstrate this effect for the rock type and range of geometries considered. Therefore, the primary finding regarding support influence on overall pillar stress-strain behavior is that the installation of a support system can enhance ductility and residual strength, mitigating pillar degradation and potentially inhibiting sudden and violent pillar failure.

Regarding support influences on local stability, the results confirm that rockbolts are ineffective at retaining fractured material at the pillar side walls once spalling initiates. In contrast, the installation of wire mesh with face plates and rockbolts not only enhances ductility, but also retains fractured rock along the periphery. This in turn increases confinement and inhibits fracture growth and dilatancy deeper within the pillar (Kaiser et al., 1996; Colwell and Mark, 2005). In addition to ultimately leading to improved ductility and residual strength as noted above, the reduced size of the zone of loosened and fractured rock helps to mitigate hazards associated with pillar degradation and associated falls of ground.

7. Conclusions

Prior studies on pillar behavior have largely focused on in-situ observations, where conducting truly controlled experiments is often difficult, and on small-scale laboratory testing, where uncertain scale effects limit our ability to extrapolate findings to actual mining conditions. This research reports the results of a series of large-scale laboratory compression tests on a porous limestone block to analyze rock behavior and rock-support interaction at a large scale (edge length of 0.5 m) with different w/h ratios. Based on the results of this study, the following conclusions were drawn:

(1) For the unsupported specimens, both peak and residual strengths increased with w/h ratios. However, the peak strength remained unchanged with the addition of rockbolts and wire mesh for the respective w/h ratios. The post-peak behavior became more ductile with the addition of support, and the residual strength increased accordingly. This is due to the passive nature of the grouted rockbolt, which provides resistance to the specimens' deformation when cracks begin to form and dilate (i.e. starting between CD and the point of peak strength)

(2) The ROFDR-distributed optical fiber sensors provided a high spatial resolution (0.65 mm) for strain measurement of rock and rockbolt deformation, aiding in identifying localized dilatational and contractional deformation of the rock. A correlation was observed between strain localization on the specimen surface obtained from 3D-DIC, the CD threshold, and DOS strain measurement for the unsupported specimen.

(3) In specimens supported only with rockbolts, the rockbolt load mobilization was observed to be higher for the $w/h = 2$ case compared to the $w/h = 0.5$ and 1 cases; hence, the post-peak ductility and residual strength substantially increased for specimens with $w/h = 2$.

(4) With the installation of wire mesh and a single rockbolt with face plates, the residual strength and ductility of the specimens with $w/h = 1$ increased. However, the post-peak behavior of the $w/h = 0.5$ specimens was not affected. This is because although the surface support prevented spalling and degradation of the specimens in both cases, it did not inhibit the shear failure mechanism of the $w/h = 0.5$ specimen.

(5) Empirical pillar strength formula does not account for post-peak behavior and support effects. This limitation could result in a conservative pillar design, potentially leading to low ore recovery and consequently adversely impacting project economics. The findings of this study underscore the importance of incorporating considerations for post-peak behavior and rock-support interaction into the pillar design process.

Declaration of competing interest

The authors declare that they have no known competing financial interests or personal relationships that could have appeared to influence the work reported in this paper.

Acknowledgments

We acknowledge the funding support from Alpha Foundation for the Improvement of Mine Safety and Health Inc. (ALPHA-FOUNDATION, Grant No. AFC820-52). The authors would like to thank the Pittsburgh Mining Research Division, National Institute for Occupational Safety and Health (NIOSH) for providing access to the MRS facility for performing the laboratory tests. We would also like to extend our gratitude to Vincent Trinidad from RMC College for helping us set up the fiber optic sensing system.

References

Alejano, L.R., Arzúa, J., Castro-Filgueira, U., Malan, F., 2017. Strapping of pillars with cables to enhance pillar stability. J. South. Afr. Inst. Min. Metall. 117 (6), 527–540.

Alejano, L.R., Arzúa, J., Estévez-Ventosa, X., Suikkanen, J., 2020. Correcting indirect strain measurements in laboratory uniaxial compressive testing at various scales. Bull. Eng. Geol. Environ. 79, 4975–4997.

Andersson, J.C., Martin, C.D., Stille, H., 2009. The Äspö pillar stability experiment: part II—rock mass response to coupled excavation-induced and thermal-induced stresses. Int. J. Rock Mech. Min. Sci. 46 (5), 879–895.

Bahaaddini, M., Rahimi, M., 2018. Distinct element modelling of the mechanical behavior of intact rocks using Voronoi tessellation model. Int. J. Min. Geol. Eng. 52 (1), 61–68.

Bahrani, N., Hadjigeorgiou, J., 2017. Explicit reinforcement models for fully-grouted rebar rock bolts. J. Rock Mech. Geotech. Eng. 9 (2), 267–280.

Bai, Q., Tu, S., 2020. Numerical observations of the failure of a laminated and jointed roof and the effective of different support schemes: a case study. Environ. Earth Sci. 79 (10), 1–18.

Barczak, T.M., 2005. An overview of standing roof support practices and developments in the United States. In: Proceedings of the Third South. Afr. Rock. Eng. Symp., pp. 301–334. Johannesburg, South Africa.

Bhandari, A.R., Inoue, J., 2005. Experimental study of strain rates effects on strain localization characteristics of soft rocks. Soils. Found. 45 (1), 125–140.

Bieniawski, Z.T., 1968. The effect of specimen size on compressive strength of coal. Int. J. Rock Mech. Min. Sci. 5 (4), 325–335.

Blanton, T.L., 1981. Effect of strain rates from 10-2 to 10 sec-1 in triaxial compression tests on three rocks. Int. J. Rock Mech. Min. Sci. Geomech. Abstr. 18 (1), 47–62.

Cai, M., Kaiser, P.K., Tasaka, Y., Maejima, T., Morioka, H., Minami, M., 2004. Generalized crack initiation and crack damage stress thresholds of brittle rock masses near underground excavations. Int. J. Rock Mech. Min. Sci. 41 (5), 833–847.

Chaurasia, A., Walton, G., 2023. Laboratory and numerical modeling of the effects of width-to-height ratio on the strength and deformation behavior of pillars composed of porous, weak limestone. Rock Mech. Rock Eng. 57, 719–738.

Colwell, M., Mark, C., 2005. Analysis and Design of Rib Support (ADRS) A Rib Support Design Methodology for Australian Collieries.

Colwell, M.G., 2006. A Study of the Mechanics of Coal Mine Rib Deformation and Rib Support as a Basis for Engineering Design. The University of Queensland, Australia.

Darlington, W.J., Ranjith, P.G., Choi, S.K., 2011. The effect of specimen size on strength and other properties in laboratory testing of rock and rock-like cementitious brittle materials. Rock Mech. Rock Eng. 44 (5), 513–529.

Das, M.N., 1986. Influence of width/height ratio on post-failure behaviour of coal. Int. J. Min. Geol. Eng. 4, 79–87.

Dhir, R.K., Sangha, C.M., 1973. Relationships between size, deformation and strength for cylindrical specimens loaded in uniaxial compression. Int. J. Rock Mech. Min. Sci. Geomech. Abstr. 10 (6), 699–712.
Diederichs, M.S., Kaiser, P.K., 1999. Tensile strength and abutment relaxation as failure control mechanisms in underground excavations. Int. J. Rock Mech. Min. Sci. 36 (1), 69–96.
Diederichs, M.S., 2003. Manuel Rocha medal recipient rock fracture and collapse under low confinement conditions. Rock Mech. Rock Eng. 36 (5), 339–381.
Diederichs, M.S., 2007. The 2003 Canadian Geotechnical Colloquium: mechanistic interpretation and practical application of damage and spalling prediction criteria for deep tunnelling. Can. Geotech. J. 44 (9), 1082–1116.
Dunham, R.J., 1962. Classification of carbonate rocks according to depositional texture. In: Ham, W.E. (Ed.), Classification of Carbonate Rocks. AAPG, Tulsa, pp. 108–121.
Eberhardt, E., Stead, D., Stimpson, B., Read, R.S., 1998. Identifying crack initiation and propagation thresholds in brittle rock. Can. Geotech. J. 35 (2), 222–233.
Fidanboylu, K., Efendioglu, H.S., 2009. Fiber optic sensors and their applications. 5th Int. Adv. Tech. Symp. (IATS'09) 6, 2–3.
Forbes, B.J., 2020. High Spatial Resolution Measurement of Tendon Reinforcement in Underground Construction Works. Queen's University, Canada.
Forbes, B., Vlachopoulos, N., Diederichs, M.S., Hyett, A.J., Punkkinen, A., 2020. An in situ monitoring campaign of a hard rock pillar at great depth within a Canadian mine. J. Rock Mech. Geotech. Eng. 12 (3), 427–448.
Forbes, B., Vlachopoulos, N., Hyett, A.J., 2018. The application of distributed optical strain sensing to measure the strain distribution of ground support members. Facets 3 (1), 195–226.
Forbes, B., Vlachopoulos, N., Hyett, A.J., Diederichs, M.S., 2017. A new optical sensing technique for monitoring shear of rock bolts. Tunn. Undergr. Space Technol. 66, 34–46.
Gao, F., Stead, D., Kang, H., 2015. Numerical simulation of squeezing failure in a coal mine roadway due to mining-induced stresses. Rock Mech. Rock Eng. 48 (4), 1635–1645.
Ghazvinian, E., 2010. Modelling and Testing Strategies for Brittle Fracture Simulation in Crystalline Rock Samples. Queen's University, Canada. Master Thesis.
Ghazvinian, E., Diederichs, M.S., Quey, R., 2014. 3D random Voronoi grain-based models for simulation of brittle rock damage and fabric-guided micro-fracturing. J. Rock Mech. Geotech. Eng. 6 (6), 506–521.
Ghazvinian, E.P., Diederichs M, M., Labrie, D., 2012. Formalized approaches to defining damage thresholds in brittle rock: granite and Limestone. In: 46th US Rock. Mech/Geomech. Symp.
GOM, 2019. Digital Image Correlation and Strain Computation Basics. GOM, Braunschweig, Germany.
Grasselli, G., 2005. 3D behaviour of bolted rock joints: experimental and numerical study. Int. J. Rock Mech. Min. Sci. 42 (1), 13–24.
Hajiabdolmajid, V., Kaiser, P., Martin, C.D., 2003. Mobilised strength components in brittle failure of rock. Geotechnique 53 (3), 327–336.
Henkel Adhesive Technologies, 2012. Loctite 401 technical data sheet. https://next.henkel-adhesives.com/us/en/products/industrial-adhesives/central-pdp.html/loctite-401/BP000000153529.html?variantId=135429. (Accessed 15 April 2024).
Hoek, E., Martin, C.D., 2014. Fracture initiation and propagation in intact rock - a review. J. Rock Mech. Geotech. Eng. 6 (4), 287–300.
Hoepffner, R., 2008. Distributed fiber optic strain sensing in hydraulic concrete and Earth structures. Berichte Des Lehrstuhls Und Der Versuchsanstalt Für Wasserbau Und Wasserwirtschaft. Technische Universität München, Wasserbau Und Wasserwirtschaft, p. 121.
Hyett, A., Forbes, B., Spearing, S., 2013. Enlightening bolts: using distributed optical sensing to measure the strain profile along fully grouted rock bolts. Proceedings of the 32nd Int. Conf. Ground. Control. Min. 32, 107–112.
Hyett, A.J., Moosavi, M., Bawden, W.F., 1996. Load distribution along fully grouted bolts, with emphasis on cable bolt reinforcement. Int. J. Num. Anal. Meth. Geomech. 20 (7), 517–544.
Jackson, R., Lau, J.S.O., 1990. The effect of specimen size on the laboratory mechanical properties of Lac du Bonnet grey granite. International Workshop on Scale Effects in Rock Masses 165–174.
Jaiswal, A., Shrivastva, B.K., 2009. Numerical simulation of coal pillar strength. Int. J. Rock Mech. Min. Sci. 46 (4), 779–788.
Kaiser, P.K., Kim, B., Bewick, R.P., Valley, B., 2011. Rock mass strength at depth and implications for pillar design. Min. Tech. 120 (3), 170–179.
Kaiser, P.K., McCreath, D.R., Tannant, D.D., 1996. Canadian Rockburst Support Handbook. Geomechanics Research Center.
Kostecki, T., 2013. The Instrumentation of Primary Roof Bolts in a Room-And-Pillar Mine and the Modeling of Their Performance. Southern Illinois University at Carbondale, USA. Master Thesis.
Krauland, N., Soder, P.E., 1987. Determining pillar strength-from pillar failure observation. Eng. Min. J. 188 (8), 34–40.
Labuz, J.F., Biolzi, L., 2007. Experiments with rock: remarks on strength and stability issues. Int. J. Rock Mech. Min. Sci. 44 (4), 525–537.
Li, C., Stillborg, B., 1999. Analytical models for rock bolts. Int. J. Rock Mech. Min. Sci. 36 (8), 1013–1029.
Li, D., Li, C.C., Li, X., 2011. Influence of sample height-to-width ratios on failure mode for rectangular prism samples of hard rock loaded in uniaxial compression. Rock Mech. Rock Eng. 44 (3), 253–267.
Li, H.B., Zhao, J., Li, T.J., 1999. Triaxial compression tests on a granite at different strain rates and confining pressures. Int. J. Rock Mech. Min. Sci. 36 (8), 1057–1063.
Lorig, L.J., Varona, P., 2013. Guidelines for numerical modelling of rock support for mines. Ground Support 2013: Proceed. Sev. Int. Symp. Undergr. Supp. Min. Undergr. Const. 81–105.
Luna Inc., 2023. High definition 6S fiber optic strain sensors. https://lunainc.com/product/hd6s. (Accessed 15 April 2024).
Lunder, P.J., Pakalnis, R.C., 1997. Determination of the strength of hard-rock mine pillars. Cim. Bull. 90 (1013), 51–55.
Ma, S., Nemcik, J., Aziz, N., 2013. An analytical model of fully grouted rock bolts subjected to tensile load. Cons. Build. Mat. 49, 519–526.
Martin, C.D., 1997. Seventeenth Canadian geotechnical colloquium: the effect of cohesion loss and stress path on brittle rock strength. Can. Geotech. J. 34 (5), 698–725.
Martin, C.D., Chandler, N.A., 1994. The progressive fracture of Lac du Bonnet granite. Int. J. Rock Mech. Min. Sci. 31 (6), 643–659.
Martin, C.D., Maybee, W.G., 2000. The strength of hard-rock pillars. Int. J. Rock Mech. Min. Sci. 37, 1239–1246.
Medhurst, T.P., Brown, E.T., 1998. A study of the mechanical behaviour of coal for pillar design. Int. J. Rock Mech. Min. Sci. 35 (8), 1087–1105.
Modiriasari, A., Bobet, A., Pyrak-Nolte, L.J., 2017. Active seismic monitoring of crack initiation, propagation, and coalescence in rock. Rock Mech. Rock Eng. 50 (9), 2311–2325.
Mohamed, K.M., Murphy, M.M., Lawson, H.E., Klemetti, T., 2016. Analysis of the current rib support practices and techniques in US coal mines. Int. J. Min. Sci. Tech. 26 (1), 77–87.
Moore, K.S., Vlachopoulos, N., 2023. The use of an innovative fiber optic methodology to capture the axial response of rib spacing and grout annulus effects on grouted rock bolts. In: Expanding Underground-Knowledge and Passion to Make a Positive Impact on the World. CRC Press, pp. 2480–2487.
Mortazavi, A., Hassani, F.P., Shabani, M., 2009. A numerical investigation of rock pillar failure mechanism in underground openings. Comp. Geotech. 36 (5), 691–697.
Obert, L., Duvall, W.I., 1967. Rock Mechanics and the Design of Structures in Rock. Wiley, New York.
Obert, L., Windes, S.L., Duvall, W.I., 1946. Standardized Tests for Determining the Physical Properties of Mine Rock, No. 3891. US Bureau of Mines, 1946.
Olsson, W.A., 1991. The compressive strength of tuff as a function of strain rate from 10− 6 to 103/sec. Int. J. Rock Mech. Min. Sci. Geomech. Abstr. 28 (1), 115–118.
Pan, B., Qian, K., Xie, H., Asundi, A., 2009. Two-dimensional digital image correlation for in-plane displacement and strain measurement: a review. Measr. Sci. Tech. 20 (6), 062001.
Renani, H.R., Martin, C.D., 2018. Modeling the progressive failure of hard rock pillars. Tunn. Undgr. Space Tech. 74, 71–81.
Serbousek, M.O., Signer, S.P., 1987. Linear Load-Transfer Mechanics of Fully Grouted Roof Bolts, vol. 9135. US Department of the Interior, Bureau of Mines.
Shirole, D., Hedayat, A., Walton, G., 2019. Experimental relationship between compressional wave attenuation and surface strains in brittle rock. J. Geophys. Research: Solid Earth 124 (6), 5770–5793.
Shirole, D., Walton, G., Hedayat, A., 2020. Experimental investigation of multi-scale strain-field heterogeneity in rocks. Int. J. Rock Mech. Min. Sci. 127, 104212.
Signer, S.P., Cox, D., Johnston, J., 1997. A method for the selection of rock support based on bolt loading measurements. In: 16th Int. Conf. Ground Contr. Min., pp. 183–190
Sinha, S., Walton, G., 2021. Investigation of pillar damage mechanisms and rock-support interaction using Bonded Block Models. Int. J. Rock Mech. Min. Sci. 138, 104652.
Sinha, S., Walton, G., Chaurasia, A., Diederichs, M., Batchler, T., 2022. Evaluating size effects for a porous, weak, homogeneous limestone. Rock. Mech. Rock Eng. 56, 3755–3772.
Sjoberg, J.S., 1992. Failure modes and pillar behaviour in the Zinkgruvan mine. ARMA US Rock. Mech./Geomech. Symp. ARMA-92.
Sutton, M.A., Orteu, J.J., Schreier, H., 2009. Image Correlation for Shape, Motion and Deformation Measurements: Basic Concepts, Theory and Applications. Springer Sci. Busin. Media.
Trillion Quality System, 2020. Digital Image Correlation. https://www.trilion.com/technologies. (Accessed 15 April 2024).
Valiet, M. R. A. van, Mier, J. G. M. van, 1996. Experimental investigation of concrete fiacture under uniaxial compression. Mech. of Cohesive-Frictional Mat. 1, 115–127.
Vlachopoulos, N., Cruz, D., Forbes, B., 2018. Utilizing a novel fiber optic technology to capture the axial responses of fully grouted rock bolts. J. Rock Mech. Geotech. Eng. 10 (2), 222–235.
Wagner, H., 1980. Pillar design in coal mines. South. Afr. Inst. Min. Metall. 80 (1), 37–45.
Walton, G., Hedayat, A., Kim, E., Labrie, D., 2017. Post-yield strength and dilatancy

evolution across the brittle–ductile transition in Indiana limestone. Rock Mech. Rock Eng. 50 (7), 1691–1710.
Walton, G., Sinha, S., 2022. Challenges associated with numerical back analysis in rock mechanics. J. Rock Mech. Geotech. Eng. 14, 2058–2071.
Windsor, C.R., 1997. Rock reinforcement systems. Int. J. Rock. Mech. Min. Sci34 (6), 919–951.
Zhao, X.G., Cai, M., Wang, J., Ma, L.K., 2013. Damage stress and acoustic emission characteristics of the Beishan granite. Int. J. Rock Mech. Min. Sci. 64, 258–269.
Zhou, Z., Chen, L., Cai, X., Shen, B., Zhou, J., Du, K., 2018. Experimental investigation of the progressive failure of multiple pillar–roof system. Rock Mech. Rock Eng. 51 (5), 1629–1636.

Akash Chaurasia is a PhD candidate in the Mining Engineering Department. His research interests lie in Geotechnical Engineering, focusing on the computation of underground rock mechanics design, which involves stress around openings, rib/snook design, and pillar design. Currently, he is working on the pillar failure mechanism and pillar-support interaction using large-scale laboratory tests and numerical modeling.